Research Square

Preprints are preliminary reports that have not undergone peer review.
They should not be considered conclusive, used to inform clinical practice,
or referenced by the media as validated information.

Progressive Neuroinvasive and Neurodegenerative Disease Due to Potosi Virus in an Immunosuppressed Adult

Julian Villalba

jvn1987@gmail.com

Centers for Disease Control and Prevention https://orcid.org/0000-0001-9230-8747

Emily Davis

Centers for Disease Control and Prevention

Kunio Nakamura

Cleveland Clinic https://orcid.org/0000-0002-7833-8138

Justin Abbatemarco

Cleveland Clinic

Kara Swenson

Centers for Disease Control and Prevention https://orcid.org/0000-0002-7296-1316

Amanda Calvert

Centers for Disease Control and Prevention

Carolyn Gould

Centers for Disease Control and Prevention

Jennifer Kasten

Centers for Disease Control and Prevention, Division of High-Consequence Pathogens and Pathology, Infectious Diseases Pathology Branch

Mark Cohen

Case western Reserve University

Paola Loreto-Palacio

National Prion Disease Pathology Surveillance Center

Georgia Ficarra

Centers for Disease Control and Prevention

Tengguo Li

Centers for Disease Control and Prevention

Sheryll Corchuelo-Chavarro

Centers for Disease Control and Prevention https://orcid.org/0000-0003-2950-9102

Pamela Fair

Centers for Disease Control and Prevention, Division of High-Consequence Pathogens and Pathology, Infectious Diseases Pathology Branch

Marlene DeLeon-Carnes
Centers for Disease Control and Prevention, Division of High-Consequence Pathogens and Pathology, Infectious Diseases Pathology Branch

Brooke Leitgeb
Centers for Disease Control and Prevention

Kimberly Machesky
Ohio Department of Health

Carlos Isada
Cleveland Clinic

Hannah Wang
Cleveland Clinic

Sudeb Dalai
Stanford University School of Medicine

Steve Miller
Delve Bio

Robert J Fox
CCF

Gabrielle Yeaney
Cleveland Clinic

Holly Hughes
Centers for Disease Control and Prevention

Erin Staples
CDC

Aaron Brault
CDC

Julu Bhatnagar
US Centers for Disease Control and Prevention

Article

Keywords: Orthobunyavirus, Meningoencephalitis, Neurodegenerative disease, B-cell depletion

Posted Date: August 4th, 2026

DOI: https://doi.org/10.21203/rs.3.rs-9935321/v1

License: This work is licensed under a Creative Commons Attribution 4.0 International License.
Read Full License

Additional Declarations: There is **NO** Competing Interest.

Progressive Neuroinvasive and Neurodegenerative Disease Due to Potosi Virus in an Immunosuppressed Adult

Julian A. Villalba, MD[1]†; Emily Davis, PhD[2]; Kunio Nakamura, PhD[3]; Justin R. Abbatemarco, MD[4,5]; Kara Swenson, PhD[1]; Amanda E. Calvert, PhD[2]; Carolyn V. Gould, MD, MS[2]; Jennifer Kasten, MD, MSc, MSc[1]; Mark L. Cohen, MD[6,7]; Paola Loreto-Palacio, MD[6,7]; Georgia Ficarra, MS[1]; Tengguo Li, PhD[1]; Sheryll Corchuelo-Chavarro, MS[1]; Pamela Fair[1]; Marlene DeLeon Carnes[1]; Brooke Leitgeb, MSGH[1]; Kimberly D. Machesky, MPH[8]; Carlos Isada[9], Hannah Wang, MD[10]; Sudeb Dalai, MD, PhD[11,12]; Steven A. Miller, MD, PhD[11]; Robert J. Fox, MD[4,5]; Gabrielle A. Yeaney, MD[10]; Holly R. Hughes, PhD[2]; J. Erin Staples, MD, PhD[2]; Aaron C. Brault, PhD[2]; Julu Bhatnagar, PhD[1].

Affiliations:

1. Infectious Diseases Pathology Branch, Division of High-Consequence Pathogens and Pathology, National Center for Emerging and Zoonotic Infectious Diseases, Centers for Disease Control and Prevention, Atlanta, GA, USA.
2. Arboviral Diseases Branch, Division of Vector-Borne Diseases, US Centers for Disease Control and Prevention, Fort Collins, CO, USA.
3. Department of Biomedical Engineering, Cleveland Clinic Research, Cleveland Clinic, Cleveland, OH, USA.
4. Department of Neurology, Cleveland Clinic, OH, USA.
5. Mellen Center for Multiple Sclerosis, Neurological Institute, Cleveland Clinic, Cleveland, OH, USA.
6. Department of Pathology, Case Western Reserve University, School of Medicine, Cleveland, OH, USA.
7. National Prion Disease Pathology Surveillance Center, Case Western Reserve University, School of Medicine, Cleveland, OH, USA.
8. Ohio Department of Health, Columbus, OH, USA.
9. Department of Infectious Diseases, Section of Neurologic Infections, Cleveland Clinic, Cleveland, OH, USA.
10. Department of Pathology and Laboratory Medicine, Diagnostics Institute, Cleveland Clinic, Cleveland, OH, USA.
11. Delve Bio, Boston, MA, USA.
12. Stanford University School of Medicine, Stanford, CA, USA.

†To whom correspondence should be addressed:
Julian A. Villalba, M.D.
Human Diagnostic Pathology team lead
Infectious Diseases Pathology Branch
Centers for Disease Control and Prevention
1600 Clifton Rd NE, MS: H18-SB
Atlanta, GA 30329-4027
Primary email: JVillalbaNunez@cdc.gov
Phone: Tel: 404-639-8531
Cellphone: 404-374-0649

Keywords: Orthobunyavirus, Meningoencephalitis, Neurodegenerative disease, B-cell depletion.

Abstract

Potosi virus (POTV), an orthobunyavirus first isolated in 1989, has been detected in multiple mosquito species across the United States, but its pathogenic potential in humans remains uncertain. Here we report the first in-depth pathological and pathogenetic characterization of POTV central nervous system (CNS) infection manifesting as rapidly progressive dementia in a woman receiving long-term rituximab therapy. Antemortem metagenomic next-generation sequencing (mNGS) of cerebrospinal fluid detected POTV in the setting of progressive brain volume loss on longitudinal neuroimaging, culminating in death almost a year after symptom onset. Comprehensive postmortem neuropathological examination demonstrated diffuse meningoencephalitis with widespread spongiform neurodegeneration and evidence of POTV infection throughout all evaluated CNS subregions (n=75), with detectable viral replication in 80% of subregions. Quantitative spatial and machine learning–based analyses demonstrated marked regional heterogeneity in viral burden, with the highest genomic POTV RNA levels in the cerebellum ($p<0.0001$), where viral RNA density correlated with spongiosis and severe Purkinje and granule cell loss (ρ up to 0.39; $p<0.001$). Hierarchical clustering identified distinct CNS compartments characterized by chronic infection and progressive neurodegeneration, while comparative sequencing demonstrated intrahost viral variation with region-specific mutations. Collectively, these findings demonstrate that POTV can cause persistent CNS infection associated with progressive neurodegeneration in B-cell–depleted hosts, raising the possibility that chronic viral infection may underlie a subset of transmissible dementia-like syndromes and highlighting the need to consider emerging arboviruses in unexplained neurodegenerative disease.

Target Journal: Nature Communications
Abstract word count: 230 words
Manuscript word count: 3,303 words

Main

Members of the genus *Orthobunyavirus* in the family *Peribunyaviridae* are arthropod-borne, enveloped viruses with segmented, single-stranded, negative-sense RNA genomes. Several of these species are known to cause neurological disease in humans and animals[1]. Potosi virus (POTV), an orthobunyavirus in the Bunyamwera serogroup first isolated from *Aedes albopictus* mosquitoes in Missouri in 1989, has since been detected in multiple mosquito species across several U.S. states[2], with white-tailed deer experimentally implicated as the primary reservoir hosts[3]. POTV RNA was recently detected in cerebrospinal fluid (CSF) from a patient on rituximab with progressive neurological decline[4], but its role in human disease remains unclear. As an emerging and rare arboviral disease, POTV infection remains poorly characterized, and to date no detailed description of its pathogenesis, viral cellular localization, or intra-host evolution in human tissues has been reported. Here, we present a fatal case of human POTV meningoencephalitis manifesting as progressive dementia, with diffuse central nervous system (CNS) neurodegeneration confirmed at autopsy. Through detailed spatiotemporal characterization of viral distribution and intra-host viral variation, we provide critical insights into potential mechanisms underlying viral associated neurodegeneration.

Results

Case Study

In early January 2025, a 37-year-old woman from Ohio with multiple sclerosis (MS), diagnosed in 2011 and treated with rituximab (last infusion, November 2024), presented with dizziness, unsteady gait, dysarthria, limb incoordination, impaired judgment, dysphagia, emotional lability, and word-finding difficulty. In retrospect, her family recalled intermittent cognitive decline and emotional and behavioral changes beginning in summer 2024. Magnetic resonance imaging (MRI) showed moderate global parenchymal volume loss compared with imaging obtained one year earlier, without new demyelinating lesions.

She was hospitalized in early April 2025 with worsening symptoms and episodic confusion. Neurologic examination revealed intact orientation to person, place, and time, global hyperreflexia, and limb and truncal cerebellar ataxia. The lumbar puncture demonstrated mild lymphocytic pleocytosis (6 nucleated cells per microliter, 90% lymphocytes, 7% monocytes, and 3% neutrophils), glucose level of 58 mg/dL, and elevated total protein level of 62 mg/dL. Repeat MRI demonstrated continued cerebral and cerebellar atrophy without new T2 hyperintensities or contrast enhancing lesions. She was empirically treated for presumed MS relapse with intravenous pulse methylprednisolone without improvement.

She was readmitted later that month with intermittent fever, worsening confusion, hallucinations, and catatonic posturing. Five days after admission, she developed an *Escherichia coli* urinary tract infection and was treated with ceftriaxone. She underwent 6 cycles of electroconvulsive therapy without clinical improvement. Repeat MRI demonstrated continued CNS atrophy progression, including the cerebellum. CSF real-time quaking-induced conversion was negative for pathogenic

prion protein, but markers of neuronal injury were markedly elevated in CSF, including 14-3-3γ (84,936 AU/mL; reference range: 173-1,999 AU/mL) and T-tau protein (14,180 pg/mL; reference range: 0-1,149 pg/mL). She was transferred to the neurointensive care unit, where she remained febrile, exhibiting rising creatine kinase levels, and electroencephalographic features of global encephalopathy. Whole blood flow cytometry analysis showed 0% CD3-CD19+ lymphocytes (reference range: 5-22%). Comprehensive CSF microbiological testing remained negative. In early May, metagenomic next-generation sequencing (mNGS) of CSF detected POTV with 2,982 sequence reads aligning to viral L, M and S segments out of 49,194,101 total RNA reads (Delve Bio, Inc., MA). The patient was transitioned to hospice care and subsequently died; a brain-only autopsy was performed. A timeline of the patient's clinical course and key interventions is shown in **Figure 1A**.

Longitudinal Volumetric Neuroimaging

We performed a longitudinal volumetric analysis in four clinical MRIs (Jan 2024, Jan 2025 [first clinical presentation], April 2025 [POTV diagnosis], and May 2025) using computational volumetric methods to assess regional brain changes over time. Marked progressive atrophy was observed in all measured tissue compartments over the 16-month interval, with caudate and putamen exhibiting the greatest cumulative volume loss (>25%; **Figure 1B**). As a proportion of total volume loss, cerebellar grey matter, caudate, cerebral cortical grey matter, and putamen showed the greatest atrophy progression over the first interval (64%-80%; Jan 2024 to Jan 2025), representing the earliest regions of atrophy. Cerebellar white matter showed the greatest atrophy progression during the middle interval (58%; Jan 2025 to April 2025), followed by the thalamus, hippocampus, and cerebral white matter during the final interval (Apr 2025 – May 2025; **Figure 1C**).

Postmortem examination

Following written permission from the family, a limited brain-only autopsy was performed. On gross examination, the brain weighed 1,085 g, at the lower end of the expected range for an adult woman. There was mild-to-moderate symmetric enlargement of the lateral ventricles. Sagittal sections showed mild, symmetric superior cerebellar atrophy, readily apparent grossly. The leptomeninges showed small patches of recent subarachnoid hemorrhage (<5 cc each) in the right frontal, left temporal, and bilateral occipital lobes. Overall, findings were consistent with generalized cerebral atrophy and secondary ventricular enlargement, indicative of *hydrocephalus ex vacuo* (**Figure 2A-B**, **Supplementary Figure 1, Supplementary Table 1**).

Neuropathological examination showed severe cerebellar neurodegeneration (**Figure 2C**), *status spongiosis* involving cortical grey matter (**Figure 2D**), and neuron-containing regions throughout the CNS. Vacuolar alterations were accompanied by marked neuronal loss, neuronal dystrophy, and secondary white-matter degeneration. These findings occurred in a background of diffuse meningoencephalitis and rhombencephalitis, with pervasive microglial activation (**Figure 2E**), neuronophagia, and neuronal satellitosis (**Figure 2F**). Prion protein (PrP) immunostaining was negative in all tissue sections. Bacilliform intravascular colonies were identified across multiple CNS regions and confirmed as *Escherichia coli* by wide-range pan-eubacterial 16S rRNA gene PCR and immunohistochemistry (IHC; **Supplementary Figure 2**). Bacterial spillage into the cerebral parenchyma was detected and accompanied by microgliosis and phagocytic uptake.

Postmortem examination determined fulminant encephalitis with diffuse neurodegeneration as the primary cause of death, with subarachnoid hemorrhages and *Escherichia coli* sepsis contributory to the cause of death.

POTV infection across CNS regions

Comprehensive histomorphometric profiling across CNS anatomical regions demonstrated regional heterogeneity in viral burden, microglial activation, and neuronal loss (**Figure 3A**). POTV RNA was detected in nearly all examined CNS anatomical regions and subregions (n=74/75, 98.7%) by in-situ-hybridization (ISH) targeting genomic RNA segments (S-sense and L-sense) encoding the POTV nucleoprotein and RNA-dependent RNA polymerase. POTV antigens were detected in all regions (n=75/75, 100%) by IHC using a cross-reactive monoclonal antibody against the orthobunyavirus nucleoprotein. Both techniques demonstrated widespread viral protein and RNA within different cell types and in the surrounding extracellular space (**Figure 2G-J**). Tissue-optimized POTV-specific RT-PCR was positive in RNA extracted from all FFPE tissue samples (**Supplementary Figure 3**).

Regional variation in POTV Viral RNA burden

Machine-learning-derived quantitative mapping of ISH signals using pixel classifiers demonstrated variation of POTV genomic RNA (vRNA) density ($POTV_{RNA\text{-}index}$) across the CNS (p<0.0001, **Supplementary Figure 4**). The cerebellum, particularly the granule cell layer (GCL), exhibited the highest vRNA density, exceeding all other regions (p<0.0015, **Figure 3A-C**). Elevated levels were also observed in subcortical and cortical regions, including the basal ganglia and temporal cortex, whereas lower levels were seen in meningeal, hippocampal, and subependymal compartments. Neuroanatomical compartmentalization explained a substantial proportion of variability in POTV vRNA density in regression analyses (R^2=0·44, p<0·0001), and these differences persisted after adjustment for quantitative measures of replication, inflammation and neurodegeneration (**Supplementary Tables 2-4**), indicating a non-uniform regionally patterned distribution of infection.

Determinants of POTV replication

Viral replication, assessed by ISH targeting POTV replicative subgenomic RNA intermediates, was detectable in most CNS regions (80%, 60/75), but at lower levels than vRNA (**Supplementary Figure 4C-E**). Replication density, quantified using a machine-learning derived pixel classification of replicative ISH signals ($POTV_{Rep\text{-}index}$), was associated with vRNA density (p=0·002), though anatomical factors explained a limited proportion of its variability (R^2=0·16; p=0·03, **Supplementary Tables 2 and 5**). A replication efficiency index, representing replication relative to total viral burden (log-scale difference between replication density and total genomic RNA density), also showed regional variation (R^2=0·18; p<0·0001) (**Supplementary Table 6**). These findings suggest that viral replication varies across regions, even after adjusting for active microglial inflammation.

Host inflammatory response and neurodegenerative changes.

Widespread microglial activation was observed across CNS regions, with prominent microglial nodules seen in multiple areas (**Figure 2E**). Digital histomorphometric analysis of Iba1 IHC whole-slide images demonstrated significant regional variation in microglial density, with the highest levels in the pons, periaqueductal, and subependymal subregions, and the lowest in the cerebellum (p<0·0001; **Supplementary Figure 5**). Peri-neuronal inflammation, (assessed using a semiquantitative score [NPS*score*] capturing immune cell clustering around neurons and neuronal engulfment), also varied significantly across subregions and was the lowest in the cerebellum (p<0·0001; **Supplementary Figure 5**).

In contrast, neurodegenerative changes showed an inverse pattern. Quantitative assessment of neuronal loss (assessed using a semiquantitative score [NL*score*]) by digital histomorphometry showed significant regional differences across the CNS. Tissue spongiosis (vacuolation), quantified using a rule-based pixel classification, also varied significantly across regions, with both measures

highest in the cerebellum (p<0·0001; **Figure 3C**; **Supplementary Figure 5**). The *ChronicDamage* score, a composite histomorphometric index integrating injury magnitude and spatial homogeneity as described in *Methods*, confirmed that chronic tissue injury was most severe in the cerebellum relative to other CNS regions (*p*<0·0001; **Figure 3C**). Notably, neurodegenerative changes were also prominent in selected hippocampal subregions (e.g., subiculum).

Viral antigen is enriched at CSF-adjacent clearance niches

To quantify the extent of viral nucleoprotein antigen density across the CNS, we calculated a standardized index of POTV viral antigen per mm2 of tissue ($POTV_{Ag\text{-}index}$). The $POTV_{Ag\text{-}index}$ varied significantly across neuroanatomical regions (p<0.0001) and was enriched at CSF interfaces including leptomeninges, ventricular surfaces, and choroid plexus. Histopathological comparison of IHC and ISH slides demonstrated a spatial dissociation between viral antigen and replication density ($POTV_{Rep\text{-}index}$), with strongly immunoreactive phagocytic cells seen near CSF spaces despite limited replication signals (**Supplementary Figure 6**). IHC also highlighted immunoreactive neurons and glial cells (**Figure 2G-I**).

Anatomical compartmentalization and CSF proximity (a strong independent predictor) explained nearly half of the variability in viral nucleoprotein antigen density (R^2=0·48, p<0·0001), even after accounting for cerebral inflammation; whereas vRNA and replication measures alone explained little variance (R^2=0·09, p<0·05; **Supplementary Tables 7-8**). An antigen discordance index (*AgResidual*) quantifying antigen enrichment relative to viral RNA and replication signals as described in *Methods*, confirmed our histopathological observations that viral antigen predominantly localized to CSF-adjacent regions (**Supplementary Figure 6**). AgResidual also varied across regions after adjustment for microglial inflammation (R^2=0.34; p<0.0001, **Supplementary Table 9**). These data indicate that antigen distribution reflects both viral activity and local phagocytic clearance.

Neurodegeneration is associated with regional POTV viral burden

Histopathological evaluation showed that grey matter regions with marked neuronal loss and vacuolation had high levels of POTV vRNA but reduced viral replication density. Quantitative analysis confirmed that viral RNA density was inversely correlated with neuronal loss (p=0·009), and markers of neuronal inflammation (neuronophagia/satellitosis; p<0·001). Regions with greater tissue vacuolation, a quantitative marker of neurodegeneration, showed proportionally lower replication efficiency (p=0·022), an association that remained significant after adjustment for neuroanatomical compartmentalization and CSF proximity (p=0·008; **Supplementary Tables 10-11**), indicating reduced replication activity in chronically injured tissue despite persistent viral RNA.

To minimise anatomical confounding, we performed ROI-focused analyses within the cerebellar GCL, the compartment with most neurons in the CNS[5] and the region with highest POTV genomic RNA burden (**Figure 3C-D**). Machine-learning based pixel classifiers were used to quantify viral RNA burden (vRNA) and tissue vacuolation (GCL*Vacuolation*), whereas deep learning–based cell detection was used to measure cellularity normalized by area (µm2) within annotated ROIs. Within the GCL, vRNA density correlated inversely with cellular density (Spearman ρ=−0·23; p=0·016;) and positively with vacuolation (ρ=0·39; p<0·001; **Figure 3D**). Because spongiosis in grey matter regions is a recognised histopathological marker of neuronal loss in neurodegenerative diseases, we modelled vacuolation as the outcome variable. Tissue vacuolation was independently associated with increased vRNA density (β=3·92; p=0·002), whereas cellular density was inversely associated with tissue vacuolation (β=−635·46; p=0·013). Notably, a significant interaction between vRNA density and cellular density (β=−218·91; p=0·013) indicated that the association between viral

burden and tissue vacuolation was strongest in regions with lower neuronal density (**Supplementary Table 12, Supplementary Figure 7**). Bootstrap resampling (2,000 iterations) yielded confidence intervals consistent with the primary model estimates (**Supplementary Table 12**). Together, these findings suggest that POTV viral burden contributes to spongiosis in the cerebellar cortex, with the magnitude of injury varying by local neuronal density.

Tissue-specific histopathologic signatures and compartments of POTV cellular infection and replication

In analyses restricted to neuron-containing anatomical regions, dimensionality reduction and unsupervised hierarchical clustering identified four tissue compartments distinguished by virologic, neuroinflammatory, and neurodegenerative features. Clusters reflected distinct biological states including (i) a post-replicative neurodegenerative compartment, (ii) an antigen-dominant clearance compartment, (iii) a replication-active inflammatory compartment, and (iv) a mixed transitional phenotype (**Figure 3E**). Similar results were observed in analyses across all CNS regions (**Supplementary Figures 8** and **9, Supplementary Tables 13-15**). Notably, cerebellar regions clustered in compartments characterized by high viral RNA burden, minimal replication activity, spongiosis, and homogeneous neuronal loss.

Mutational landscape across CNS regions

Next-generation sequencing of RNA extracted from brain tissue samples identified all three Potosi genomic segments (L, M, and S) across all brain regions tested, with broader sequence coverage of the S segment, albeit at lower depth, and more limited coverage of the L and M segments. (**Supplementary Table 16**). However, the cerebellum showed the highest breadth and depth of coverage across all three segments. Viral sequences from this patient showed genomic divergence from the historical reference POTV strain 1899 (Genebank accession numbers MF066368-MF066370; **Supplementary Table 17**).

Intrahost variability was assessed by comparing the sequence of each CNS specimen with those from the cerebellum. Several nucleotide changes were detected across all three Potosi genomic segments in sequences assembled from different postmortem samples (**Figure 4** and **Supplementary Table 18**). These data suggest intrahost variability at the consensus level across CNS regions at low frequency. However, the extent of variability may be underestimated given incomplete genome coverage.

Discussion

We present a case of Potosi virus encephalitis with rapidly progressive neurodegeneration in a patient receiving B-cell repleting monoclonal therapy for MS, resulting in death almost a year after symptom onset. This case provides the first in-depth histopathological characterization of human disease for this rare arbovirus. Although several other orthobunyaviruses have been associated with neuroinvasive disease[1] and chronic encephalitis in patients with B-cell deficiencies[4,6-8], the pathogenesis of neurodegeneration is poorly characterized. Our findings describe a fulminant, pan-neuraxial neurodegenerative and inflammatory process underlying rapidly progressive dementia, with clinicopathological features resembling spongiform encephalopathies.

Our assessment integrating orthogonal viral detection methods with quantitative image-based analytics provides evidence supporting the direct role of POTV in the observed neurodegeneration. First, vRNA and antigens were detected almost universally across the CNS, including within neuronal

cell bodies and processes, demonstrating marked neurotropism and spatial dissemination throughout the neuraxis. The concordant detection of replicative RNA intermediates and protein across independent assays strengthens the biological specificity of these findings. Second, regions with the most severe neurodegenerative changes had the highest viral burden as measured by machine-learning derived pixel-classifiers. The cerebellar grey matter was most prominently affected histologically, consistent with volumetric MRI findings showing early atrophy in this region, as well as in the cerebral grey matter, caudate, and putamen. Additionally, early cerebellar involvement aligns with the patient's initial progressive cerebellar syndrome of appendicular and truncal ataxia, gait instability, dysarthria, and vertigo. Early cerebellar involvement may also have led to altered motivational and emotional states[9,10]. Similar clinicopathological correlations included frontal lobe injury with executive dysfunction and catatonic posturing, basal ganglia pathology with hyperkinetic movements, corticospinal tract degeneration with hyperreflexia and clonus, and hippocampal injury with short-term memory impairment. Collectively, the close topographic alignment between tissue injury and neurological deficits further supports a direct link between POTV infection and the observed progressive neurological syndrome. Third, regression modeling showed that areas with advanced neuronal loss contained high levels of viral genomic RNA but reduced replication activity, suggesting persistence of viral material within chronically injured tissue following prior cytopathic effects. In contrast, regions with early neuronal injury and inflammation (e.g., neuronophagia) but without spongiosis, showed lower RNA density. Volumetric measures from longitudinal MRIs were concordant with this evolution. These findings suggest a temporally evolving host-pathogen interaction in which active infection precedes neuronal loss, followed by persistence of viral RNA in chronically damaged tissue. Finally, alternative causes of spongiform or infectious encephalopathies, including prion disease, were comprehensively excluded through extensive ancillary testing.

Several observations support the chronicity of CNS infection in this case. First, longitudinal neuroimaging and gross examination demonstrated marked and progressive brain volume loss resulting in hydrocephalus ex vacuo. Second, POTV viral burden within the cerebellar GCL correlated with histological features of neurodegeneration, with this association varying by local neuronal density, suggesting that viral-associated injury occurs alongside neuronal depletion over time. Third, quantitative viral RNA mapping integrated with hierarchical clustering revealed spatiotemporal heterogeneity across CNS compartments. Regions enriched for persistent viral RNA and neurodegenerative features were identified, particularly in the cerebellum, alongside regions with more preserved architecture exhibiting viral replication. Finally, histopathological and antigen-mapping analyses demonstrated features of phagocytic viral clearance near CSF interfaces, consistent with an ongoing post-inflammatory state. Similar patterns have been described in other orthobunyavirus infections, including mouse models of La Crosse virus[11], where neuronal infection triggers RNA helicase and mitochondrial antiviral signaling protein pathways, leading to upregulation of sterile alpha and toll/interleukin (IL-1) receptor motif-containing 1 mRNA, followed by oxidative cell damage and neuronal apoptosis. Together, these findings support a chronic neuroinvasive process in which viral replication, post-replicative vRNA persistence, and cumulative neurodegenerative injury coexist across anatomically distinct CNS regions. Notably, chronic viral meningoencephalitis with diffuse cerebral atrophy has previously been reported in association with Cache Valley virus[6.8], an orthobunyavirus of the Bunyamwera serogroup[12] that is genetically related to POTV[13].

The severity and prolonged course of infection in this patient were likely influenced by her underlying immunosuppression related to anti-CD20 monoclonal antibody therapy. Patients receiving rituximab

and other B-cell–depleting monoclonal antibodies are at increased risk of serious and opportunistic infections, including viral infections[14]. Rituximab has also been associated with rapidly progressive dementia due to JC virus-associated progressive multifocal leukoencephalopathy[15,16], and chronic enterovirus meningoencephalitis[17,18]. JC virus granule cell neuronopathy (JCV-GCN) is a rare neurological complication that has been reported in patients receiving rituximab therapy, characterized by progressive cerebellar ataxia due to lytic infection of cerebellar granule cell neurons by a mutated form of JC polyomavirus[19]. By depleting B cells and impairing humoral immunity, these therapies can inhibit viral clearance, thereby permitting prolonged viral replication, neuroinvasion, and persistent disease[20]. Consistent with this biological framework, we and others have observed that rituximab-treated patients who develop arboviral infections, including orthobunyaviruses[4,6-8], may experience protracted clinical courses with evidence of intrahost viral variation[21] and delayed or absent serologic responses[22].

The intrahost viral variation observed in this case, while it should be interpreted with caution, may support the presence of a complex host-pathogen interaction, as immunosuppressed hosts can provide a permissive environment for ongoing viral replication and diversification[23,24]. Mathematical modeling[25] and growing clinical evidence[24,26-27] suggest that such conditions may facilitate accelerated viral evolution during chronic infection. However, whether intrahost viral evolution contributed to increased pathogenicity of POTV in this patient remains unclear and warrants further investigation. Nevertheless, genomic analyses of orthobunyaviruses indicate that additional evolutionary mechanisms, including natural genome reassortment, may also contribute to viral diversification[28,29] and influence pathogenicity[30-33].

Although autopsy examination provides a single terminal snapshot of disease, the spatially resolved molecular and histopathological analyses and the longitudinal volumetric MRI measures presented here reveal marked temporal heterogeneity across CNS compartments. This heterogeneity enables inference of distinct stages of viral activity and tissue injury within the same individual, consistent with prior autopsy studies of systemic viral infections[34,35]. The pronounced spongiosis involving cerebellar and cortical grey-matter regions suggest that these areas were initially the sites of potential viral replication and cell death, and lead to some of the patient's findings early in their disease course

This fatal case demonstrates the potential of POTV for neuroinvasion and associated neurodegeneration driven by uncontrolled viral dissemination across the CNS in the setting of profound B cell depletion. Clinicians should consider POTV and other arboviruses in immunosuppressed patients presenting with rapidly progressive dementia and other neurologic symptoms. Additional studies are needed to delineate the epidemiology, risk factors for, and clinical spectrum of POTV infection.

Methods

Case Selection

We describe the pathology and laboratory testing performed in tissues from an individual with Potosi virus (POTV) infection who developed severe disease, requiring hospitalization, and subsequently died. Specimens were submitted to CDC's Infectious Diseases Pathology Branch (IDPB) on 27 June 2025 for pathology consultation and diagnostic evaluation. Available medical and autopsy records submitted as part of diagnostic consultation were reviewed. This activity was reviewed by CDC and

conducted consistent with applicable federal law and CDC policy (45 C.F.R. part 46, 21 C.F.R. part 56; 42 U.S.C. §241(d); 5 U.S.C. §552a; 44 U.S.C. §3501 et seq).

Antemortem Volumetric MRI Analysis

Four clinical MRIs were obtained (Jan 2024, Jan 2025 [first clinical presentation], April 2025 [POTV diagnosis], and May 2025). T2-weighted MRIs were used to synthesize standardized 1mm isotropic T1-weighted MRIs using generative probabilistic diffusion model. Cerebral tissues (cerebral cortical gray matter, cerebral white matter, thalamus, hippocampus, caudate, and putamen) were segmented using FreeSurfer (v7.3.2, SynthSeg)[36] and cerebellar tissues (cerebellar gray matter and cerebellar white matter) segmented using multi-atlas label fusion method[37,38]. Volumetric change was calculated using tensor-based pairwise Jacobian integration method compared to prior scan for percent volume change in each tissue[39]. Lastly, the proportion of volume change relative to the total, cumulative (Jan 2024 to May 2025) volume change was calculated for each tissue within each scanning interval.

Postmortem examination and tissue collection

Limited brain-only autopsy tissue procurement was performed using a standardized protocol to ensure comprehensive collection of organ systems at the Cleveland Clinic. Tissues were fixed in 10% neutral-buffered formalin for histological analysis. A list of all postmortem tissue samples evaluated in this study is included in **Supplementary Table 19**.

Histology. Detection of POTV and Other Infectious Agents in Tissues

Formalin-fixed, paraffin-embedded (FFPE) tissues were processed at IDPB for routine histology, sectioned at 4 µm, and stained with hematoxylin-eosin for histopathological evaluation. Tissue samples collected during autopsy (**Supplementary Table 20**) were analyzed for deep spatiotemporal characterization of POTV viral RNA/antigen distribution and intra-host viral variation as described below. Techniques included in situ hybridization (ISH) and immunohistochemistry (IHC) for POTV, reverse transcription-polymerase chain reaction (RT-PCR), and metagenomic next-generation sequencing (mNGS). Detection of other pathogens was determined by laboratory-developed IHC and tissue-based PCR assays.

Immunohistochemistry

An IHC assay for detection of orthobunyavirus antigens was performed using a mouse monoclonal anti-Cache Valley virus (anti-CVV4) antibody [CDC, Ft. Collins, CO][40.41] in combination with an indirect immunoalkaline phosphatase polymer detection system and red chromogen for visualization. Deparaffinized and rehydrated tissue sections were placed in an autostainer and digested in 0·1 mg/mL proteinase K [Millipore Sigma, St. Louis, MO]. A protein blocker, Background Punisher [Biocare Medical, Pacheco, CA] was applied to the sections for 10 min, followed by a 30 min incubation with the anti-CVV4 antibody at a dilution of 1:100. The sections were then incubated with Mach 4 Universal AP for 10 min followed by Mach 4 Universal AP Polymer for 15 min [Biocare Medical, Pacheco, CA] and finally SIGMAFAST Fast Red TR/Naphtol AS-MX [Sigma-Aldrich, Saint Louis, MO] was applied for 30 min. Slides were counterstained with Mayer's Modified Hematoxylin [StatLab, McKinney, TX], blued in Lithium blue [Polysciences, Inc., Warrington, PA], and mounted with aqueous mounting medium [BioSB, Santa Barbara, CA]. Appropriate positive and negative controls were run in parallel; negative controls used normal mouse serum in place of the primary antibody. The mouse monoclonal antibody was generated against Cache Valley virus (*Orthobunyavirus cacheense*) but is broadly reactive with other viruses of the genus *Orthobunyavirus*, including Jamestown Canyon virus (*Orthobunyavirus jamestownense*), LaCrosse virus (*Orthobunyavirus lacrosseense*),and Potosi virus

(*Orthobunyavirus potosiense*). It is shown in our laboratory not to cross-react with Oropouche virus (*Orthobunyavirus oropoucheense*). The anti-CVV4 antibody[40] has also been shown to have cross-reactivity in immunofluorescence assays (IFA) of Vero cells infected with viruses in the Bunyamwera serogroup at an MOI 1.0 and fixed 24 hours post-infection, including, Potosi virus (POTV) strain IL94-1921, Tlacotalpan virus (TLAV) strain 61D240, Fort Sherman virus (FSV) strain 86MSP18, Playas virus (PLAV) strain 75V5938Tensaw virus (TENV) strain A9-171B, Maguari virus (MAGV) strain BeAr7272, and La Crosse virus (LACV) strain Original.

In situ hybridization

To localize genomic and replicative viral RNA in FFPE autopsy tissues, three customized RNAScope POTV ISH probes (Advanced Cell Diagnostics (ACD), Newark, CA) were used. Two probes target the L segment of the viral genome (sense and antisense), and one probe targets the S segment of the viral genome (sense). The L antisense probe binds to replicative RNA intermediates, indicating replication. The ISH assays were performed on FFPE tissues by using an RNAscope 2·5 HD Red Detection Kit (ACD), following manufacturer's protocol and as described previously[42]. Briefly, deparaffinized 4 µM tissue sections were subjected to target retrieval for 15 min at 98-100°C in 1X Target Retrieval Solution, dehydration in 100% ethanol for 3 min, and Protease Plus treatment for 30 min at 40 °C in a HybEZ™ oven (ACD). Slides were subsequently incubated with a ready-to-use probe mixture for 2 h at 40 °C in a HybEZ™ oven, and the signal was amplified using a specific set of amplifiers (AMP1-6), as recommended by the manufacturer. The signal was detected using a Fast Red solution (Fast Red B: Fast Red A in a 1:60 ratio) for 10 min at room temperature. Slides were counterstained with Mayer's Modified Hematoxylin (Poly Scientific R&D Corp, Bay Shore, NY) for 2 min and blued using Lithium blue (Polysciences, Inc., Warrington, PA) for 1 min. Slides were finally mounted with Ecomount (Biocare Medical, Pacheco, CA). Appropriate positive and negative controls were run in parallel. One probe targeting the S segment of the viral genome is specific for the genus *Orthobunyavirus*, and in addition to detecting POTV, it also cross-reacted with Cache Valley virus (*Orthobunyavirus cacheense*). However, this probe did not cross-react with Jamestown Canyon virus (*Orthobunyavirus jamestownense*), and LaCrosse virus (*Orthobunyavirus lacrosseense*). Similarly, the probes targeting the L segment of the POTV viral genome did not cross react-with Cache Valley virus (*Orthobunyavirus cacheense*), Jamestown Canyon virus (*Orthobunyavirus jamestownense*), and LaCrosse virus (*Orthobunyavirus lacrosseense*).

Molecular detection of POTV in Tissues

RNA was extracted from FFPE tissues using an RNA extraction protocol, as previously described[43]. The S segment of the Potosi virus genome was selected for Potosi virus specific primers design: Potosi-Fw: 5'-TCTACCCGTTGGCAATTGGGATC-3'; Potosi-Rv: 5'-GGCTGCTGCGCTAACATTTGTT-3'. Primers were synthesized by the Biotechnology Core Facility at the CDC. The assays were performed using the OneStep RT-PCR Kit (Qiagen, Valencia, California) and 5 µL of RNA template, according to the manufacturer's instructions. The thermocycling conditions were as follows: 1 cycle at 50°C for 30 minutes, 1 cycle at 95°C for 15 minutes, then 40 cycles of incubation at 94°C, 55°C, and 72°C for 1 minute each, followed by 1 cycle of final extension at 72°C for 10 minutes. Amplification products were analyzed by electrophoresis on a 1·8% agarose gel containing ethidium bromide. Amplicons of the expected size (196bp) were gel-purified and sequenced on a GenomeLab GeXP sequencer (AB SCIEX, Redwood City, California). Sequence homologies were assessed using the Basic Local Alignment Search Tool (BLAST) against the NCBI nucleotide database (http://blast.ncbi.nlm.nih.gov/Blast.cgi). A specimen was considered positive for Potosi virus only if the amplicon sequence demonstrated ≥98% nucleotide identity with reference Potosi virus sequences.

Whole-slide imaging acquisition
All slides were scanned using a Leica Aperio AT2 whole-slide scanner (Leica Biosystems) under identical acquisition conditions. Images were acquired at an apparent magnification of 40x with a spatial resolution of 0·2519 µm per pixel, as recorded in the image metadata. Whole-slide images (WSIs) were stored in SVS format with JPEG compression and tiled image organization. Image visualization and quantitative assessment were performed using Aperio ImageScope software (v12.4.6.50003), preserving native image resolution and calibration metadata for all analyses.

Testing for coinfections and other histopathologic processes.
To evaluate for the presence of coinfecting pathogens, IHC and tissue-based PCR assays were performed for various infectious agents as warranted, based on histopathologic findings. An *Escherichia coli* IHC assay was used in this study to confirm the presence of the pathogen in all CNS regions. Prion protein (PrP) immunostaining was performed to exclude the presence of pathogenic misfolded prion. In addition, IHC for cellular markers were performed to better categorize the histopathology of other alternate non-infectious histopathological processes. Evaluated cellular markers included CD20, Ionized calcium-binding adaptor molecule 1 (Iba1), and NeuN. Primary antibodies and pretreatments are provided in **Supplementary Table 21**. Wide-range eubacterial Gram-negative and Gram-positive bacteria 16S rRNA gene PCR assays were performed as previously described[44] on DNA extracted from FFPE tissues with histopathological evidence of bacterial infection. DNA extracted from FFPE tissue was also used as a template for an *Escherichia coli*/*Salmonella*/*Shigella* multiplex PCR assay targeting the *uidA*, *invA*, *ipaH* (186bp, 284bp, 401bp, respectively). Housekeeping genes for this multiplex assay are *β-globin* (500bp) and *GAPDH* (200bp).

Histopathological evaluation and histomorphometry

Overview of analytical framework
We performed histopathological evaluation using a multimodal, next-generation pathology framework developed for this study. This framework combined expert classical histopathological interpretation and pathologist-derived histomorphometric assessment with quantitative image-based analytics. The latter included rule-based and machine-learning–based pixel classification methods applied to regions-of-interest (ROI). Our approach enabled precise and reproducible quantification of viral distribution and pathological hallmarks of tissue injury across 75 CNS neuroanatomical regions. This multimodal approach leveraged the strengths of neuropathology expertise for complex morphologic features (neuronal loss, neuronophagia, and neuronal satellitosis), while harnessing high-resolution computational methods for objective spatial and quantitative analysis (quantification of in-situ hybridization signals and tissue vacuolation), providing a comprehensive and high-precision characterization of disease-associated pathology.

The histomorphometric approach included three components. First, four pathologist-derived measures were assessed, including two quantitative indices (POTV antigen density per mm^2 of tissue [$POTV_{Ag\text{-}index}$] and microglial density [$Iba1_{index}$]), and two semi-quantitative scores (neuronal loss [NL *score*], and neuronophagia-neuronal satellitosis [NPS *score*]). Second, a rule-based pixel classifier was used to derive a quantitative index of vacuolar (spongiotic) degeneration ($Vacuolation_{index}$). Third, two machine-learning–based pixel classifiers that quantified total genomic viral RNA density ($POTV_{RNA\text{-}index}$) and viral replication density ($POTV_{Rep\text{-}index}$) from ISH signals targeting the S (sense) and L (antisense) gene segments respectively.

Additionally, we derived three model-based quantitative indices to better understand viral pathogenesis. The antigen discordance index (*AgResidual*) represents the residual antigen signal after accounting for regional genomic RNA and replication densities. *AgResidual* reflects whether a region contains more or less viral antigen than would be expected based on its measured viral RNA profile. The replication efficiency index (*RepEff*) is the log-scale difference between replication density and total genomic RNA density. *RepEff* reflects how much active replication is occurring relative to the total amount of virus present in each region. To integrate histopathological findings associated with neurodegeneration, we derived a composite chronic injury score (*ChronicDamage*), incorporating both the magnitude and spatial distribution of neuronal loss and spongiotic degeneration.

Lastly, to identify histopathological features associated with viral tropism and replication, we fit multivariable linear regression models with log-transformed $POTV_{RNA\text{-}index}$, $POTV_{Rep\text{-}index}$, and $POTV_{Ag\text{-}index}$ as dependent variables. Independent variables included quantitative histomorphometric indices and semiquantitative scores of histological findings commonly reported in CNS viral infections (e.g., microglial density), as well as categorical neuroanatomical variables.

Histopathological Evaluation

We systematically recorded the presence or absence of a predefined set of histopathological features across all neuroanatomical regions and subregions of each postmortem specimen using a multimodal histopathological assessment framework. A total of 75 CNS anatomical regions and subregions were evaluated, encompassing cortical and cerebellar laminae (e.g., cerebellar Purkinje cell layer), white-matter tracts (e.g., optic radiations), ventricular and subependymal zones, leptomeninges, and brainstem nuclei and pathways. The presence or absence of selected histological features was annotated without formal grading. A complete list of evaluated CNS neuroanatomical regions and subregions is provided in **Supplementary Table 19**. A list of histopathological features recorded in CNS neuroanatomical regions and subregions is provided in **Supplementary Table 20**.

CNS functional system classification

We classified the 75 CNS regions and subregions into eight nominal categories termed “CNS functional systems” based on shared histological architecture, neuroanatomical organization, and pathophysiological roles. This categorization grouped anatomically distinct structures according to common cellular composition, connectivity patterns, and vulnerability profiles, facilitating interpretation of region-specific pathological changes across H&E-stained sections from the frontal lobe, basal ganglia/insula, hippocampal formation and temporal lobe, pons (middle–upper), and cerebellum. The nominal categories included 1) ventricular system / ependymal structures, 2) leptomeninges, 3) non-cortical integrative systems / nuclei, 4) hippocampal formation, 5) basal ganglia / subcortical nuclei, 6) cortical area (neocortex/allocortex), 7) white matter tracts / interconnection, and 8) cerebellar cortex. Ventricular and leptomeningeal compartments were analyzed separately given their specialized epithelial or mesenchymal histology and because of their specialized roles in CSF dynamics, immune surveillance, and neuroinflammatory responses. Overall, this categorization integrated histological features with functional neuroanatomy to provide a pathophysiologically meaningful framework for regional analysis.

Morphometric analyses

We employed a multimodal approach to characterize histopathological features within the CNS microarchitecture. This approach included: (1) pathologist-driven histomorphometry, incorporating

manual and digital methods to derive quantitative indices and semi-quantitative scores; (2) a computational, rule-based pixel quantification approach to derive a quantitative index of tissue vacuolation; and (3) machine-learning–based pixel classification to generate quantitative indices of viral RNA burden and viral replication.

Pathologist-driven histomorphometry

In contrast to the spatially complex and highly heterogeneous signal patterns observed with in situ hybridization in CNS tissues, IHC detection of Orthobunyavirus viral protein produced discrete, cell-associated signals that are largely confined to the soma or cytoplasm of neurons and glial cells, as well as the cytoplasm or nuclei of endothelial and inflammatory cells. Iba1 also produces discrete, cell-associated signals confined to the cytoplasm of glial cells. Because these signals can be readily attributed to individual cells and lack the axonal or punctate patterns characteristic of ISH, a pathologist-driven manual histomorphometric approach was employed to quantify antigen-positive cells. This strategy leverages expert recognition of CNS cytology to ensure accurate cell identification and attribution of signal in the setting of complex tissue architecture, while allowing reliable exclusion of nonspecific staining or background reactivity that is more effectively resolved by human interpretation than by automated classification without extensive model training.

Manual Histomorphometry

IHC-stained slides of each specimen were quantitatively scored for a histomorphological numerical index of viral antigen burden (see next section) by one board-certified anatomic pathologist with expertise in infectious diseases pathology. Histopathological evaluations were performed with a ZEISS Axio Imager M1 upright brightfield microscope with fully motorized stage interfaced to a digital camera (AxioCam MRc5, Carl Zeiss, Inc.), and equipped with 5x, 10x, 20x, 40x, and 63x dry objective lenses along with a 100x (oil) immersion objective. The field-of-view number of the eyepieces PL 10x/25 Br. foc. and E-PL 10x/25 Br. foc. is 25 mm. The 63x objective used for numeric morphometric quantitation is Carl Zeiss AG Objective EC Plan-Neofluar 63x/0,95 Korr M27 (Item no.: 420380-9970-000). We calculated the Field of view diameter (FOV⌀) for the objective used in this study with the following formula[45]:

$$FOV\varnothing = \frac{FN}{OM}$$

Where FN is field number of the ocular, and OM is objective magnification. The ZEISS Axio Imager M1 FN is 25, and the OM used in this study for histomorphometric analysis was 63x. The resulting FOV⌀ used in this study was 0·397 millimeters.

We calculated the area of a high-power field (HPFA) used in this study with the following formula[45]:

$$\underline{HPF_A = \pi FOVr^2}$$

Where $FOVr$ is the field of view radius. The resulting ZEISS Axio Imager M1 HPF_A used in this study with a 63x objective is 0·124 mm^2 (10 HPF = 1·24 mm^2).

POTV antigen density ($POTV_{Ag\text{-}index}$) and POTV antigen spatial variability ($POTV_{Ag\text{-}SD}$)

We developed one numeric index to measure the number of cells displaying POTV antigen by orthobunyavirus (OBV) IHC assay. The index was calculated using the following formula:

Tissue sections were stained by an OBV IHC assay for the detection of POTV viral antigen as described above, and antigen-positive cells were manually quantified by a pathologist. The tissue antigen density was expressed as the number of positive cells per mm^2 of tissue. The $POTV_{Ag\text{-}index}$ represents the mean number of IHC positive cells by an OBV IHC assay per 10 high-power-fields (HPF, at 63x objective magnification = 1·24 mm^2). To count IHC positive cells in IHC-stained slides, a pathologist selected 3-4 hotspot regions and performed cellular quantification in 2-4 consecutive fields within each hotspot region (for a total of up to 10 hotspot fields). The index was calculated as follows:

$$POTV_{Ag-index} = mean\ Orthobunyavirus_{IHC+cells/10HPF} = \frac{1}{10}\sum_{n=1}^{10} C_n$$

Where:

- C_n= number of OBV IHC–positive cells in HPF n

To capture field-to-field spatial variation in antigen distribution, viral antigen spatial variability *($POTV_{Ag\text{-}SD}$)* was calculated as the standard deviation of immunoreactive cell counts across the same 10 HPFs.

$$\sigma = POTV_{Ag-SD} = \sqrt{\frac{1}{9}\sum_{n=1}^{10}\left(C_n - POTV_{Ag-index}\right)^2}$$

Where:

- C_n= number of OBV IHC–positive cells in HPF n
- $POTV_{Ag-index}$ = Mean number of positive cells per HPF across the 10 fields

Digital histomorphometry

WSIs of hematoxylin-eosin stained and immunohistochemistry-stained sections were generated and analyzed for digital histomorphometric quantification of cellular antigen burden or semiquantitative assessment of specific histopathological features (see next sections). Digital histomorphometry was performed using Aperio ImageScope software (v12.4.6.50003; Leica Biosystems). Quantitative assessment was conducted at an apparent magnification of 40× using a fixed digital viewport.

Each digital high-power field (D-HPF) corresponded to a fixed screen viewport measuring 1,073 × 654 pixels at 40× magnification. Using scanner calibration metadata (microns per pixel [MPP] = 0·2519 µm/pixel), the area of a single D-HPF was calculated and applied consistently across all specimens for numeric index derivation. Each D-HPF covered an area of approximately 0·04453 mm^2. Counts were obtained from up to 10 non-overlapping D-HPFs per section, yielding a total analyzed tissue area of 0·4453 mm^2. ImageScope window size and panel layout were kept constant during all scoring.

Microglial density index ($Iba1_{index}$) and microglial density spatial variability ($Iba1_{SD}$)
Whole-slide images of Iba1-immunostained sections were acquired using a Leica Aperio AT2 scanner and analyzed using Aperio ImageScope software (v12.4.6.50003). Quantification was performed at 40x digital magnification. Microglial burden was assessed by manual counting of Iba1-positive cells within hotspot regions. For each section, 3–4 hotspot regions were selected, and cellular quantification was performed in 2–4 consecutive, non-overlapping digital high-power fields (D-HPFs) per hotspot, for a total of up to 10 D-HPFs per section.

The microglial density index ($Iba1_{index}$) was defined as the mean number of Iba1-positive cells per D-HPFs across the 10 evaluated fields and calculated as:

$$Microglial\ density\ index = Iba1_{index} = \frac{1}{10}\sum_{n=1}^{10} C_n$$

Where:

- C_n= represents the number of Iba1-positive cells in the n^{th}D-HPF.

To capture field-to-field spatial heterogeneity in microglial distribution, microglial spatial variability was calculated as the sample standard deviation of Iba1-positive cell counts across the same 10 D-HPFs:

$$Iba1_{SD} = \sqrt{\frac{1}{9}\sum_{n=1}^{10}(C_n - \mathrm{Iba1_{index}})^2}$$

Semiquantitative histologic grading
We graded all CNS neuronal cell body–containing neuroanatomical regions and subregions (n=42) by two non-severity histomorphological scoring systems. Non-severity semiquantitative scoring data were collected by a board-certified anatomic pathologist in WSIs in 10 D-HPFs, each corresponding to a fixed screen viewport measuring 1,073 × 654 pixels at 40× magnification as described. A summary of the semiquantitative scores is provided in **Supplementary Table 22.**

Neuronal loss score (NL score) and Neuronal loss spatial variability (NL_{SD})
Neuronal loss was evaluated in neuron-containing neuroanatomical regions and subregions within hotspot areas. For each region/subregion, three to four hotspot areas were randomly selected, and cellular quantification was performed in two to four consecutive, non-overlapping D-HPFs per hotspot, for a total of up to 10 D-HPFs per section. Neuronal loss was assessed semiquantitatively based on the estimated proportion of dead neurons per field using a three-tiered scoring system: mild neuronal loss (≤20%), moderate neuronal loss (20–79%), and severe neuronal loss (≥80%), corresponding to scores of 1, 2, and 3 points, respectively. A neuronal loss score was calculated as the mean semiquantitative neuronal loss category across the 10 D-HPFs, providing a summary measure of neuronal loss severity within each region or subregion. Neuronal loss score variability (NL_{SD}) was calculated as the standard deviation of neuronal loss scores across the 10 D-HPFs, reflecting spatial variability in neuronal loss severity within the sampled tissue.

Neuronophagia and Neuronal satellitosis score (NPS score) and Neuronophagia and neuronal satellitosis spatial variability (NPS_{SD})

Neuronophagia and neuronal satellitosis were assessed semiquantitatively in neuron-containing neuroanatomical regions and subregions within hotspot areas. For each region or subregion, three to four hotspot areas were randomly selected, and cellular assessment was conducted in two to four consecutive, non-overlapping D-HPFs per hotspot, for a total of up to 10 D-HPFs per section.

In each D-HPF, foci of neuronophagia and/or neuronal satellitosis were jointly scored using a five-tiered semiquantitative scale: score 1, no active foci; score 2, very rare (1 focus); score 3, rare (2–3 foci); score 4, abundant (4–9 foci); and score 5, diffuse (>10 foci). A neuronophagia–satellitosis score (NPS *score*) was calculated as the mean semiquantitative category across the 10 D-HPFs, providing a summary measure of the severity of neuron-associated glial reactions within each region or subregion. Neuronophagia–satellitosis spatial variability (NPS_{SD}) was calculated as the standard deviation of scores across the 10 D-HPFs, reflecting spatial variability in these histopathological features within the sampled tissue.

Neuronophagia was defined as a histopathological process characterized by the engulfment and digestion of injured or dead neurons by activated microglial cells, appearing as clusters or rosettes of microglia surrounding and phagocytosing a degenerating neuron, often with loss of normal neuronal architecture and pyknotic nuclei. Neuronal satellitosis was defined as the close apposition of non-phagocytic glial cells, most commonly oligodendrocytes or astrocytes, around an intact or only mildly injured neuronal soma, forming a ring-like arrangement of evenly spaced glial nuclei without evidence of neuronal necrosis or phagocytosis, consistent with a reactive or supportive glial response.

Rule-based pixel quantification

Because both spongiform change within neuron-containing regions and secondary white-matter degeneration result in expansion of fluid-containing spaces within the CNS parenchyma, these pathological processes produce a common histological signature on hematoxylin–eosin–stained sections, manifested as increased near-white areas within the tissue. Given the diffuse, spatially heterogeneous, and morphologically consistent nature of these vacuolar changes, a computationally derived, rule-based pixel quantification approach was employed to estimate the burden of tissue vacuolation and edema. This strategy allowed objective, reproducible quantification of vacuolar change across neuroanatomical regions by leveraging the consistent optical properties of fluid-filled spaces on routine histological staining.

Tissue vacuolation index ($Vacuolation_{index}$)

To quantify increased fluid-containing spaces within the CNS parenchyma characteristic of spongiform change and secondary white-matter degeneration (Wallerian degeneration), digital microphotographs were acquired from each central nervous system (CNS) neuroanatomical region and subregion excluding the leptomeninges (10 images per region/subregion; 70 regions/subregions; 700 images total). Images were selected by a board-certified pathologist at 40x magnification using ImageScope, with a fixed on-screen viewport to ensure consistent field selection. Areas affected by tissue-processing artifacts, including regions of tissue lifting or separation related to sectioning, were excluded from image acquisition. Areas including large cerebral vessels were also excluded to avoid large vascular lumina. All captured images had identical pixel dimensions (1,716 x 1,013 pixels), ensuring uniform spatial sampling across regions and subregions.

Tissue vacuolation was estimated using a custom Python version 3.13 image analysis script generated by Claude-Sonnet 4.5 (Anthropic) that quantified all pixels in an image with red, green, and blue (RGB) values between 235 and 255. These pigment values are consistent with near-white regions on hematoxylin-eosin-stained sections, corresponding to fluid-filled spaces.

The tissue vacuolation index was calculated as the proportion of pixels meeting these criteria relative to the total number of pixels per image *i*, with values then averaged across the 10 images for each region or subregion to generate the $\text{Vacuolation}_{index}$.

$$Parenchymal\ vacuolation\ index = Vacuolation_{index} = \frac{1}{10}\sum_{i=1}^{10} V_i$$

Where:

- V_i = represents the vacuolation proportion for image i.

This approach provided a reproducible, region-specific estimate of vacuolar burden across heterogeneous patterns of spongiform change and secondary white-matter degeneration. As a morphology-based metric, the $\text{Vacuolation}_{index}$ does not distinguish the underlying histopathological mechanism and reflects the overall burden of parenchymal rarefaction and fluid-filled space expansion in both grey and white matter.

To capture field-to-field spatial heterogeneity in tissue vacuolation, the spatial variability of tissue vacuolation ($Vacuolation_{SD}$) was then defined as the sample standard deviation of these image-level proportions.

$$Vacuolation_{SD} = \sqrt{\frac{1}{9}\sum_{i=1}^{10}(V_i - \text{Vacuolation}_{\text{index}})^2}$$

For quantitative assessment of tissue vacuolation, we applied the rule-based pixel quantification exclusively to parenchymal regions. Leptomeninges and choroid plexus were excluded because they are non-parenchymal compartments and do not exhibit true parenchymal vacuolation on histological examination; inclusion of these structures would therefore confound interpretation of spongiform change. For this specific analysis, the CNS regions were reorganized into “CNS neuroanatomical groups,” which largely parallel but do not completely replicate the previously defined “CNS functional systems”. This slight modification was intentional and driven by pathophysiological considerations.

The primary objective of this reclassification was to distinguish intrinsic grey matter vacuolation—occurring within neuron-containing regions—from secondary white matter degeneration (e.g., Wallerian degeneration), which predominantly affects myelinated axonal tracts. Because the cellular composition, microarchitecture, and mechanisms of injury differ fundamentally between neuronal somatodendritic compartments and myelin-rich axonal compartments, separating grey matter from white matter structures was necessary to avoid conflating distinct pathological processes. The

cerebellar white matter was also analyzed separately from other major white matter tracts, mainly because on histopathological examination the pathologist observed more pronounced white matter degeneration in the cerebellar white matter, and also to capture regional differences in axonopathic patterns of vacuolation. Brainstem nuclei and the dentate nucleus were included within non-cortical integrative systems/nuclei as grey matter structures with high neuronal density, while the basal ganglia/subcortical nuclei were retained as a distinct group due to their characteristic cytoarchitecture and vulnerability profiles. Additionally, the subependymal zone (restricted to parenchyma immediately adjacent to the ventricles) was analyzed as a separate category because of its unique microenvironment, including proximity to cerebrospinal fluid and distinct cellular composition, which may influence edema formation and periventricular vacuolation. Thus, while the CNS neuroanatomical groups closely resemble the broader CNS functional systems, this classification was tailored specifically to study the microstructure of tissue vacuolation. The complete list of regions and their corresponding classification according to both CNS functional systems and CNS neuroanatomical groups is provided in **Supplementary Table 23**.

Machine learning derived pixel classifiers

Unlike the relatively uniform optical properties of fluid-filled spaces on routine histological staining, chromogenic ISH signals exhibit substantial spatial, chromatic, and contextual heterogeneity within complex CNS microenvironments. Viral RNA–associated signals vary in intensity, morphology, and local tissue context, and may overlap visually with endogenous pigments (e.g., hemosiderin), tissue debris, or sectioning artifacts, limiting the reliability of purely rule-based or threshold-driven approaches. This heterogeneity is particularly pronounced in the CNS, where viral RNA signals can extend along neuronal somata, dendrites, and axons, appear as fine punctate labeling within the neuropil, manifest as spindle-shaped isolated signals within white-matter tracts, or present as round or amorphous cytoplasmic or nuclear signals in neurons and glial cells, depending on the infected cell type and microanatomical context. To address this complexity, supervised, machine-learning–based pixel classification was employed, enabling context-aware discrimination of true viral RNA signals from background tissue and artifacts, while preserving sensitivity to biologically relevant signal variation across neuroanatomical regions.

POTV RNA density ($POTV_{RNA\text{-}index}$) and POTV Replication density ($POTV_{Rep\text{-}index}$)

POTV viral RNA genomic burden and viral replication were quantified using supervised, machine-learning–based pixel classification applied to in situ hybridization (ISH) images. Digital ISH images were analyzed using QuPath software (version 0.6.0). For each image, regions of interest (ROI) corresponding to specific CNS neuroanatomical regions and subregions were manually annotated using QuPath's annotation tools by a board-certified pathologist to delineate areas of interest prior to analysis. A total of 75 ROIs were annotated corresponding to all CNS neuroanatomical regions and subregions listed in **Supplementary Table 19**. Of note, annotations were not performed in areas of the CNS microarchitecture affected by tissue-processing artifacts, including regions of tissue lifting or separation related to sectioning.

A pixel classifier was trained to categorize individual pixels into one of three classes: "POTV signals", representing intense chromogenic signals associated with hybridization of either sense (targeting POTV genomic RNA at the S gene segment) or antisense probes (targeting replicative RNA intermediates of the L gene segment); "Brown/Black", representing pigment artifacts, tissue debris, or section folds; and "Other", representing background tissue and non-specific staining. The inclusion of a dedicated "Brown/Black" class was necessary because brown-to-black pigments

exhibited color characteristics overlapping with the chromogenic red-pink signals associated with viral RNA detection, which otherwise resulted in elevated false-positive classifications.

For classifier training, 50 manual annotations were drawn for each class. A moderate analysis resolution was selected to balance sensitivity and specificity. Higher resolutions increased false-positive classifications by capturing faint, nonspecific pigmentation, whereas the selected resolution minimized spurious signal detection while preserving robust identification of biologically relevant viral RNA signals. The classifier was trained on a representative ISH image and subsequently applied uniformly to all remaining images to ensure analytical consistency across samples.

The final classification was applied within ROIs to produce high-resolution detailed quantitative measurements across defined neuroanatomical microarchitectural compartments, such that one classifier was used throughout. QuPath was used to calculate the total area occupied by each pixel class within each annotated region. Quantitative classification data within ROIs were used for morphometrical determination of two quantitative indices: the POTV RNA density ($POTV_{RNA\text{-}index}$) and POTV Replication density ($POTV_{Rep\text{-}index}$). Each index was defined as the proportion of pixels classified as "POTV signals" relative to the total annotated tissue area within the ROI. Signals from the S sense probe were used to generate the $POTV_{RNA\text{-}index}$. Signals from the L antisense probe were used to generate the $POTV_{Rep\text{-}index}$. These indices represent the density of ISH viral RNA signal per unit area (ISH/μm^2). Together, these indices provide quantitative, machine-learning–derived measures of viral RNA genomic burden and active viral replication, respectively.

Antigen discordance index (AgResidual)

Because IHC intracellular viral antigen signals may reflect both intracellular viral protein expression or extracellular or phagocytised antigens within microglia/macrophages, we derived an "antigen discordance" metric to quantify antigen levels exceeding (or falling below) those expected from viral RNA measurements. To derive the metric, we built a predictive model of antigen discordance index (*AgResidual*) to examine whether excess antigen might reflect engulfed viral material from prior injury, in addition to active protein synthesis in infected cells. POTV RNA genomic density ($POTV_{RNA\text{-}index}$) and POTV replication density ($POTV_{Rep\text{-}index}$) were quantified as described above using whole-region pixel classification across each anatomically defined ROI (75 different neuroanatomical regions and subregions). In contrast, viral antigen abundance ($POTV_{Ag\text{-}index}$) was assessed as described above as a pathologist-driven manual histomorphometric index. These three variables ($POTV_{RNA\text{-}index}$, $POTV_{Rep\text{-}index}$, $POTV_{Ag\text{-}index}$) were measured in the 75 neuroanatomical CNS regions and subregions. Because these metrics are on different scales and are right-skewed (and may include zeros), we log10-transformed them after adding a small constant (half the minimum positive value per variable) before modeling, as described below:

For each metric $X \in \{POTV_{RNA-index}, POTV_{Rep-index}, POTV_{Ag-index}\}$, we defined a constant c_x as follows:

$$c_x = \frac{1}{2}\min\{X_i \mid X_i > 0\}$$

Where:

- X_i = represents the smallest positive value of X across all neuroanatomical regions and subregions

Calculating a defined c_x ensures $X_i + c_x > 0$, even when $X_i = 0$, and keeps constant small relative to observed positive values. The constant was defined for each of the measured variables:

$c_{RNA} = for\ POTV_{RNA\text{-}index}$
$c_{Rep} = for\ POTV_{Rep\text{-}index}$
$c_{Ag} = for\ POTV_{Ag\text{-}index}$

We defined transformed variables as follows:

$$POTV^*_{RNA} = log_{10}(POTV_{RNA-index} + c_{RNA})$$

$$POTV^*_{Rep} = log_{10}(POTV_{Rep-index} + c_{Rep})$$

$$POTV^*_{Ag} = log_{10}(POTV_{Ag-index} + c_{Ag})$$

Where:

- The superscript $*$ indicates the log-transformed scale

We next modeled the expected transformed antigen abundance $POTV^*_{Ag}$ as a function of transformed RNA and replication measurements:

$$POTV^*_{Ag} = \beta_0 + \beta1\ POTV^*_{RNA} + \beta2\ POTV^*_{Rep} + \varepsilon_i)$$

Where:

- β0 = intercept (baseline expected antigen when $POTV^*_{RNA}$ and $POTV^*_{Rep}$ are zero on the transformed scale).
- β1 = association between antigen and RNA burden, adjusted for replication.
- β2 = association between antigen and replication intermediates signal, adjusted for burden.
- εi = residual (the part of antigen not explained by $POTV^*_{RNA}$ and $POTV^*_{Rep}$).

We fit this model using **ordinary least squares (OLS)** across all regions with non-missing values. The model produces a predicted value for each region:

$$\widehat{POTV^*_{Ag}} = \beta_0 + \beta1\ \widehat{POTV^*_{RNA}} + \beta2\ \widehat{POTV^*_{Rep}}$$

Finally, the antigen discordance metric (*AgResidual*) was defined as the region-specific residual as follows:

$$AgResidual = POTV^*_{Ag} - \widehat{POTV^*_{Ag}}$$

In other words, the *AgResidual* represents the observed transformed antigen minus predicted transformed antigen. Positive *AgResidual* values indicate antigen abundance exceeding that predicted by whole-region RNA burden and replication signal (antigen "excess"). Plausible biological explanations include phagocytic uptake of antigen, persistence of antigen following earlier viral replication, antigen accumulation within immune clearance compartments, or regional differences in protein clearance. In contrast, negative *AgResidual* values indicate antigen levels lower than expected given the RNA signal. Potential interpretations include RNA persistence without active or proportional protein production (e.g., quiescent or abortive infection) or the presence of residual RNA in chronically damaged tissue. Technical factors affecting antigen and/or viral RNA detection may also influence model estimates and should be considered as possible limitations when interpreting antigen residual values. Because POTV antigen quantification ($POTV_{Ag\text{-}index}$) was based on microanatomical field sampling as defined above (10 HPFs), whereas POTV RNA genomic burden ($POTV_{RNA\text{-}index}$) and POTV replication ($POTV_{Rep\text{-}index}$) were quantified across the full ROIs, *AgResidual* captures local antigen enrichment/concentration or depletion relative to macro-scale RNA distribution and was used as a derived marker of antigen–RNA mismatch in subsequent analyses. In other words, *AgResidual* may reflect immune-mediated antigen accumulation or clearance within specific microdomains. All analyses to derive the *AgResidual* score were performed using Python 3.11. Scripts were generated by GPT-5.3 (OpenAI).

Replication efficiency index (RepEff)

To better distinguish between simple viral RNA persistence and ongoing viral activity, we developed a replication efficiency index (RepEff), which represents the log-scale difference between the regional signal for replicative RNA intermediates, also known as POTV replication density ($POTV_{Rep\text{-}index}$, marker of active viral replication), and the total genomic viral RNA density ($POTV_{RNA\text{-}index}$) within each region. In practical terms, *RepEff* reflects how much active replication is occurring relative to the total amount of virus present in each region. POTV RNA genomic density ($POTV_{RNA\text{-}index}$) and POTV replication density ($POTV_{Rep\text{-}index}$), were quantified as described above using whole-region pixel classification across each anatomically defined ROI (75 different neuroanatomical regions and subregions). To accommodate zero values and reduced right-skewness, each variable was log10-transformed after addition of a small constant. This process was done as defined above in the section described as *AgResidual* computations.

Replication efficiency (RepEff) for region i was defined as the difference between transformed replication signal and transformed RNA genomic burden:

$$RepEff_i = POTV^*_{Rep} - POTV^*_{RNA}$$

Equivalently, using log rules:

$$RepEff_i = log_{10}\left(\frac{POTV_{Rep-index} + c_{Rep}}{POTV_{RNA-index} + c_{RNA}}\right)$$

Thus, *RepEff* is mathematically equivalent to the log10 ratio of replicative RNA intermediates signals to genomic RNA burden. Positive *RepEff* values indicate disproportionally high replication relative to RNA burden (replication-permissive compartments), whereas negative values indicate RNA persistence with comparatively low replication activity (replication-constrained or quiescent compartments). *RepEff* was used as a region-level proportional activity metric in subsequent

analyses. All analyses to derive the *RepEff* score were performed using Python 3.11. Scripts were generated by GPT-5.3 (OpenAI).

Chronic damage consolidation score (*ChronicDamage*)
To operationalize a region-level histopathological signature of consolidated chronic tissue injury, we constructed a composite chronic damage consolidation score (*ChronicDamage*) integrating injury magnitude and spatial homogeneity. For each CNS region *i*, the proportion of tissue vacuolation or spongiform change was quantified using a rule-base pixel classifier which yielded the vacuolation index ($Vacuolation_{index}$) as defined above, and its within-region variability of tissue vacuolation ($Vacuolation_{SD}$). In neuron-containing regions, neuronal injury was quantified by semiquantitative neuronal loss scoring as defined above (*NL score*), and its within-region variability (NL_{SD}). Neuronal metrics were considered biologically undefined in non-neuron containing regions and were therefore not imputed.

To combine variables measured on different scales, each component was standardized using z-scores. For each variable *X*, we computed:

$$z(X_i) = (X_i - \mu_x) / \sigma_x$$

Where:

- μ_x and σ_x denote the mean and standard deviation across the relevant analysis set respectively.
- i CNS neuroanatomical region or subregion of interest

The chronic damage consolidation score (*ChronicDamage*) was then defined as:

$$ChronicDamage_i = z(Vacuolation_{index\,i}) - z(Vacuolation_{SD\,i}) + z(NL\ score_i) - z(NL\ SD_i)$$

Thus, *ChronicDamage* increases with greater injury magnitude (higher vacuolation and neuronal loss) and decreases with greater spatial heterogeneity (higher within-region standard deviations). Higher values of *ChronicDamage* were interpreted as indicating consolidated, relatively homogeneous chronic injury, where lower values were interpreted as reflecting less severe and/or more ongoing spatially heterogeneous injury patterns consistent with temporally mixed or evolving pathology. Because *ChronicDamage* is a standardized composite, values represent relative differences between regions and are not interpretable as an absolute measure of disease duration. All analyses to derive the *ChronicDamage* score were performed using Python 3.11. Scripts were generated by GPT-5.3 (OpenAI).

Multiple linear regression and residual diagnostics
We analyzed quantitative indices from 75 CNS neuroanatomical compartments using multiple linear regression to examine associations between POTV RNA density ($POTV_{RNA\text{-}index}$), antigen density ($POTV_{Ag\text{-}index}$), replication density ($POTV_{Rep\text{-}index}$), and replication efficiency (*RepEff*) levels, and selected histological and/or neuroanatomical variables. Continuous variables were log10-transformed where appropriate to reduce skewness and facilitate interpretation.

CNS functional systems, proximity to cerebrospinal fluid interfaces, microglial density ($Iba1_{index}$), tissue vacuolation ($Vacuolation_{index}$), and CNS neuroanatomical groups (only in models assessing tissue vacuolation) were evaluated as explanatory variables in prespecified models. Multivariable

models were constructed to assess the independent contributions of anatomical, viral, and inflammatory factors.

All models were estimated using ordinary least squares (OLS) regression with the HC3 heteroskedasticity-consistent covariance matrix estimator (MacKinnon & White, 1985) to account for potential variance heterogeneity across regions. Regression coefficients represent adjusted associations. Model fit was assessed using R^2, adjusted R^2, and Akaike's Information Criterion corrected for small samples (AICc). Full model diagnostics are shown within each supplementary table describing the model results. Statistical significance was defined as two-sided p<0·05. Analyses were conducted at the regional level (n=75; n=42 for neuron-restricted analyses; n= 70 tissue-vacuolation restricted analyses). Multiple linear regression analyses were conducted using GraphPad Prism (v.10.4.2).

Intra-host phenotypic characterization and unsupervised compartment discovery

To reduce the complexity of heterogeneous histopathological findings and to identify shared histopathological patterns and potential common disease mechanisms across CNS neuroanatomical regions and subregions, we applied hierarchical clustering analysis following dimensionality reduction of the full CNS multi-region histopathological dataset. This approach enabled an unbiased assessment of cross-tissue similarities, allowing for the identification of latent patterns and POTV disease-associated features that may transcend individual region/subregion pathology. All analyses and visualizations were performed using Python 3.11 with the following packages: pandas, numpy, scikit-learn, scipy, matplotlib, and seaborn. Scripts were generated by GPT-5.3 (OpenAI).

Variable selection for principal component analyses

Quantitative histopathological data were collected from 75 CNS microarchitectural compartments as described in prior sections. Prior to principal component analysis (PCA), each variable was standardized to z-scores across included regions to harmonize differences in scale and variance.

We first performed PCA analysis in neuron-containing regions to identify dominant axes of variation across regions/subregions using 12 quantitative variables representing: POTV RNA genomic density ($POTV_{RNA\text{-}index}$), POTV replication density ($POTV_{Rep\text{-}index}$), POTV antigen density and spatial variability ($POTV_{Ag\text{-}index}$, $POTV_{Ag\text{-}SD}$), microglial activation and spatial variability ($Iba1_{index}$, $Iba1_{SD}$), neuronal loss score and neuronal loss score variability (*NL score*, NL_{SD}), Neuronophagia-Satellitosis score and Neuronophagia-Satellitosis spatial variability (*NPS score*, NPS_{SD}), and tissue vacuolation index and spatial variability of tissue vacuolation ($Vacuolation_{index}$, $Vacuolation_{SD}$).

Because neuronal loss and neuronal injury metrics (neuronophagia/satellitosis) are biologically undefined in non-neuron containing regions, we then performed a PCA in non-neuron-containing regions using the other eight quantitative variables: POTV RNA genomic density ($POTV_{RNA\text{-}index}$), POTV replication density ($POTV_{Rep\text{-}index}$), POTV antigen density and spatial variability ($POTV_{Ag\text{-}index}$, $POTV_{Ag\text{-}SD}$), microglial activation and spatial variability ($Iba1_{index}$, $Iba1_{SD}$), and tissue vacuolation index and spatial variability of tissue vacuolation ($Vacuolation_{index}$, $Vacuolation_{SD}$).

Hierarchical clustering on PCA scores

For unsupervised phenotypic compartment discovery, we performed agglomerative hierarchical clustering using Ward's minimum variance method on the top three principal component (PC1-PC3) scores (**Supplementary tables 13-15**). The number of clusters (k) was selected using a combination

of dendrogram linkage distance structure (largest increase in merge height consistent with an elbow (**Supplementary figures 6-7**) and internal cluster validation (silhouette analysis across a range of k values). Cluster assignments were then mapped back to CNS neuroanatomical regions and subregions for downstream biological interpretation and later enrichment with anatomical nominal variables.

ROI-focused analyses within the cerebellar granule cell layer (GCL)

We performed region-of-interest (ROI)-focused analyses within the cerebellar granule cell layer (GCL) to investigate the relationship between POTV RNA density ($POTV_{RNA\text{-}index}$), cellular density, and tissue vacuolation. Cellularity was quantified as described below. For this specific GCL-specific analysis, tissue vacuolation was measured differently than previously described. We used different statistical methods to investigate the associations between these quantitative measures as described below.

Data collection

Two digital ISH whole-slide images of cerebellar FFPE tissue sections stained by a laboratory-developed ISH assay targeting POTV genomic RNA at the S gene segment, were analyzed using QuPath software (version 0.6.0). One WSIs contained tissue of the cerebellar vermis and the hemispheres, and the other WSI contained tissue of the cerebellar lingula. For each image, a board-certified anatomic pathologist annotated a total of 108 regions of interest (ROI) prior to analysis. ROI corresponded to areas of the GCL within the cerebellar vermis (n = 50), cerebellar hemispheres (n = 50), and cerebellar lingula (n = 8).

Cellularity quantification in GCL ROIs

The imaging analysis software QuPath (v0.6.0) was used to quantify tissue cellularity in ISH whole-slide images. Briefly, ISH images were imported into QuPath, and ROI were manually annotated within the cerebellar GCL by a board-certified pathologist. Cell detection was then performed using the StarDist2D extension with the pretrained "he_heavy_augment.pb" model for brightfield images (available via the QuPath GitHub repository)[46,47]. This cell detection approach was normalized by area (μm^2) in each annotation. This approach enabled quantification of the number of cells per unit area (cells/μm^2) within each annotated ROI. The cell detection approach was applied across all 108 annotations.

Quantification of tissue vacuolation in GCL ROIs

A pixel classifier was subsequently trained at moderate resolution to categorize image pixels in the cerebellum into two classes: "Background" and "Tissue." For training, 50 annotations per class were generated with the "Background" class defined using white regions of the image, whereas the "Tissue" class comprised areas containing nuclei and other visible tissue (corresponding to hematoxylin-stained regions). The trained classifier was then applied to quantify the total area of "Background" and "Tissue" within each annotated ROI in the ISH images. Tissue vacuolation in the GCL (GCLVacuolation) was then calculated as the proportion of pixels classified as "background" relative to the total number of pixels within each ROI. The classifier was applied across all 108 annotations.

Quantification of POTV RNA in GCL ROIs

The POTV RNA density *($POTV_{RNA\text{-}index}$)* was quantified as previously described. However, for this analysis, classification was applied to each of the 108 annotations within the CGL. In this context, the $POTV_{RNA\text{-}index}$ represents the density of ISH viral RNA signal per unit area within the GCL (ISH/μm^2).

In contrast, other cerebellar measurements included a single annotation per CNS subregion. This more extensive analysis was performed in the same ROIs used to assess cellularity and GCL vacuolation, enabling direct comparison of these three metrics within the GCL.

Correlation analyses

Associations between POTV RNA density ($POTV_{RNA\text{-}index}$, ISH/μm^2), cellular density (Cells/μm^2), and tissue vacuolation ($Vacuolation_{index}$) were evaluated in pairwise correlation analyses using Spearman's rank correlation. Spearman correlation was chosen because the ISH measurements were right-skewed and included zero values, violating the normality assumptions required for Pearson correlation. Scatterplots were performed to visualize the relationships between variables, and locally weighted regression (LOWESS) smoothing was applied to illustrate non-parametric trends without imposing a linear model. Statistical analyses, scatterplots and LOWESS curves were generated using GraphPad Prism (v.10.4.2).

Interaction model

Multiple linear regression models were fit using OLS to evaluate whether the association between viral RNA density and tissue vacuolation was moderated by cellular density. Because POTV ISH measurements were highly right-skewed and included zero values, POTV RNA density ($POTV_{RNA\text{-}index}$) was log-transformed prior to regression modeling using log10(ISH/μm^2 + 1×10^{-6}). The small constant prevents undefined values for zero measurements while having negligible impact on non-zero values. The primary multiple linear regression model evaluated whether the relationship between viral density and tissue vacuolation was moderated by cellular density. The dependent variable was Vacuolation Index. We created an interaction term, computed as the product of log-transformed $POTV_{RNA\text{-}index}$ and cellular density in each specific ROI. The interaction term tests whether the effect of viral burden on tissue vacuolation differs across levels of cellular density. The primary model was as follows:

$$Vacuolation_{Index\,i} = \beta_0 + \beta 1 \cdot log_{10}(POTV_{RNA-index\,i} + 10^{-6}) + \beta 2 \cdot Cells_i + \beta 3 \cdot [log_{10}(POTV_{RNA-index\,i} + 10^{-6}) \times Cells_i] + \varepsilon_i)$$

Where:

i : Cerebellar granule cell layer region of interest (ROI).

β_0, Intercept of regression model: representing the expected $Vacuolation_{index}$ when all predictors equal zero.

β_1, Main effect of viral burden: Represents the expected change in $Vacuolation_{index}$ associated with a one-unit increase in log-transformed viral signal when cellular density is held constant.

β_2, Main effect of cellular density: Represents the expected change in $Vacuolation_{index}$ associated with a one-unit increase in cellular density when viral burden is held constant.

β_3, Interaction coefficient between viral burden and cellular density: Represents how the effect of viral burden on vacuolation changes as cellular density varies. A significant interaction term indicates that the relationship between viral burden and tissue vacuolation depends on the local cellular density.

$Cells_i$: Cellular density (Cells/μm^2) measured in ROI *i*.

ε_i : Residual error term representing unexplained variation in $Vacuolation_{index}$ for ROI *i*.

Variance inflation factors (VIF) were calculated to assess multicollinearity among predictors. Model fit was summarized using R^2 and adjusted R^2. To quantify the unique explanatory contribution of each predictor, partial R^2 values were computed by comparing the full model with reduced models in which each predictor was sequentially removed. Robust regression using a Huber M-estimator was

additionally performed as a sensitivity analysis to reduce the influence of potential outliers. To evaluate robustness of coefficient estimates without relying on normality assumptions, non-parametric bootstrap resampling was performed with 2,000 iterations. For each iteration, ROIs were resampled with replacement, and the regression model was refit. Empirical bootstrap distributions were used to calculate mean estimates, standard deviations, and percentile-based 95% confidence intervals.

To visualize the interaction between viral burden and cellular density, a marginal effects plot was generated from the fitted interaction model. The outcome variable was the vacuolation index ($Vacuolation_{index}$), and predictors included log-transformed viral burden, cellular density, and their interaction term. Viral RNA density ($POTV_{RNA\text{-}index}$, ISH/μm^2) was transformed as log10(ISH/μm^2 + 1×10^{-6}) to accommodate right-skewness and zero values. Predicted vacuolation values were calculated from the fitted regression equation across the observed range of log-transformed $POTV_{RNA\text{-}index}$ while holding cellular density at three representative values: mean cellular density, one standard deviation below the mean, and one standard deviation above the mean. These three prediction lines were plotted to illustrate how the association between viral burden and vacuolation changes as a function of cellular density.

Statistical analyses for the interaction model analyses were performed using Python (statsmodels library, SciPy), and scripts were generated by GPT-5.3 (OpenAI).

Metagenomic next generation sequencing and genomic analysis of POTV tissue specimens
To assess intra-host viral variation across tissues, we performed comparative genomic analyses on POTV sequences obtained from postmortem samples from five neuroanatomical regions and compared those to sequences from a historical POTV sequence available on NCBI GenBank, and to a sequence detected in the cerebellum.

RNA was extracted from small (0.1 mg) sections of frozen, homogenized tissue. Random hexamer priming was used to generate mNGS libraries, which were sequenced using the NextSeq1000 platform as previously described[48]. Briefly, complementary DNA (cDNA) by using the Ovation RNA-Seq System V2 (Tecan Life Sciences, https://lifesciences.tecan.comSequencing libraries by using the NDNAPrepLibrary Prep Kit (Illumina, https://www.illumina.com) and IDT DNA/RNA UD indexes (IDT, https://www.idtdna.com).

De novo assembly was completed using SPAdes version 3.15.3 (https://github.com/ablab/spades) and its RNA viral presets. The resulting contigs were investigated for viral origin by using the viral_nt database and CLI of BLASTn version 2.12.0 (https://ftp.ncbi.nlm.nih.gov/blast/executables/LATEST) and confirmed using the nucleotide BLAST database (https://blast.ncbi.nlm.nih.gov). These *de novo* consensus sequences were then used to generate a reference guided assembly using Bowtie2 version 2.2.5 (https://github.com/BenLangmead/bowtie2) using very-sensitive-local presets. Samtools version 1.15.1 (https://github.com/samtools/samtools/releases) was used to sort reads by coordinate, from which duplicates were removed using Picard version 2.23.0 https://github.com/broadinstitute/picard/releases). Average coverage per base was calculated using using Bamtools version 2.5.2 (https://github.com/pezmaster31/bamtools).

Use of Large Language Models (LLMs)
Use of LLM-assisted approaches are described in the relevant Methods sections where applicable. LLM tools (GPT-5.5; OpenAI) were also used to assist with language editing and readability

enhancement. All scientific content, analyses, interpretations, and conclusions were developed, reviewed, and verified by the authors.

Statistical analysis

Descriptive summary statistics were summarized and analyzed using Microsoft Excel, and the results reported as mean ± one standard deviation (SD). A non-parametric Kruskal-Wallis with Dunn's post-hoc test was used to compare more than two independent groups of equal or different sample sizes. The Mann–Whitney U test was used for two-group comparisons of continuous variables. Differences were considered significant for p-values<0.05. Heatmaps and bar graphs displaying quantitative and semiquantitative indices were generated using GraphPad Prism (v.10.4.2).

Figure Legends

Figure 1. Clinical and radiological timeline of disease course.
(A) Gantt-style chart depicting the patient's dynamic course of illness highlighting clinical events (red bars), care level/disposition (blue bars), treatments (green bars), diagnostic procedures (yellow bar, lumbar puncture procedures) and cerebrospinal fluid (CSF) testing (yellow bar, metagenomic NGS testing) from initial presentation to death. Horizontal colored bars represent the duration of clinical elements including discrete interventions, and diagnostic milestones. **(B)** Percent change in volume across central nervous system (CNS) neuroanatomical compartments over a 16-month interval. Magnetic resonance imaging (MRI) was performed at four timepoints: Jan 2024, Jan 2025 (first clinical presentation), April 2025 (POTV diagnosis), and May 2025. Measured tissue compartments included cerebral cortical grey matter, cerebral white matter, cerebellar grey matter, cerebellar white matter, caudate nucleus, putamen, hippocampus, and thalamus. Values represent percent change relative to baseline (Jan 2024). Volumetric change was calculated using tensor-based pairwise Jacobian integration method compared to prior scan for percent volume change in each tissue. **(C)** Proportional contribution of regional volume loss over time. Heatmap showing the proportion of total cumulative volume loss (Jan 2024–May 2025) occurring within each MRI interval for each CNS neuroanatomical region. Values in each cell represent the percentage contribution of that interval to total volume loss for the given region, with percentages summing to 100% across intervals for each region. Color intensity reflects the magnitude of proportional volume loss.

Figure 2. Neuropathological features, and immunohistochemical and in-situ hybridization findings in POTV infection.
(A-B) Gross appearance of the brain at postmortem examination. **(A)** External view of the intact brain prior to sectioning. Inferior (basal) view of the intact brain showing preserved overall configuration with mild widening of the cerebral sulci consistent with diffuse brain atrophy. The circle of Willis and major basal vessels are identified and appear patent without gross atherosclerosis or aneurysm. The brainstem and cerebellum are unremarkable in contour but show mild symmetric atrophy. Patchy dark-red foci consistent with subarachnoid hemorrhages are present over the cortical surfaces, most prominently along the left temporal (one focus) region, but also present in the right frontal lobe (two foci) and bilateral occipital lobes (one focus each). **(B)** Representative coronal section of the cerebral hemispheres. The brain shows reduced overall volume with symmetric enlargement of the lateral ventricles, consistent with hydrocephalus ex vacuo. **(C-F)** Microscopic examination of CNS tissues demonstrated status spongiosis in the setting of diffuse meningoencephalitis and rhombencephalitis. **(C)** Cerebellar cortical tissues (vermis and hemispheres) showing severe cerebellar cortical degeneration with near-complete loss of Purkinje cells, prominent Bergmann gliosis, diffuse vacuolation and neuronal loss within the granular cell layer, and vacuolar degeneration of the molecular layer; hematoxylin–eosin stain, original digital magnification ×176. **(D)** Frontal lobe cortical grey matter demonstrating widespread spongiotic degeneration resembling a spongiform encephalopathy, with numerous small, round to oval vacuoles (approximately 2–10 μm in diameter) distributed throughout the neuropil. These impart a characteristic sponge-like

appearance and are associated with neuronal loss. Mild leptomeningeal, parenchymal, and perivascular lymphocytic inflammation is also present; hematoxylin–eosin stain, original digital magnification ×84. **(E)** Putamen showing a prominent microglial nodule associated with neuronal death, neuronophagia, and accompanying lymphocytic inflammation. Similar microglial nodules were observed throughout the neuraxis; haematoxylin–eosin stain, original digital magnification ×176. **(F)** High-power view of frontal cortical grey matter illustrating neurons undergoing neuronophagia and neuronal satellitosis, features consistently observed across neuron-containing regions of the CNS; haematoxylin–eosin stain, original digital magnification ×400. **(G-I)** Immunohistochemistry testing using an antibody raised against the orthobunyavirus nucleoprotein, highlighted viral antigens in multiple cell types across the CNS, including neurons, endothelial cells, neuroepithelial and glial cells, macrophages (Supplementary Figure 4), among other cells across the CNS, with representative examples shown in the **(G)** pontine nuclei neurons, **(H)** choroid plexus, and **(I)** subependymal zone of the lateral ventricle. **(J)** In-situ hybridization with probes targeting the S segment of the viral genome (sense), and the L segment of the viral genome (sense and antisense), demonstrated the presence of viral RNA in multiple cells and in the extracellular spaces in all CNS subregions evaluated.

Figure 3: Regional heterogeneity of Potosi virus infection across the human CNS with prominent association to neurodegenerative changes in the cerebellum. (A) Heatmap showing marked regional heterogeneity in viral burden (POTV antigen and RNA indices), viral replication (subgenomic RNA intermediates, $POTV_{Rep\text{-}index}$), microglial activation ($Iba1_{index}$ and $Iba1_{SD}$), neuronal loss (NL*score*, NL*spatial-variability*), neuronal inflammation (NPS*score*. NPS*spatial-variability*), and neurodegenerative changes ($Vacuolation_{index}$, $Vacuolation_{SD}$, *ChronicDamage*), across 75 sampled CNS subregions within the frontal lobe, basal ganglia, hippocampus/temporal lobe, pons, and cerebellum. Rows represent anatomical subregions and columns represent histomorphometric and quantitative indices. **(B)** Representative histological images of ISH-stained sections of the granule cell layer of the cerebellum, illustrating POTV RNA detection (red puncta). Sections show variable burden and distribution of signal across regions, with lower density in areas with preserved architecture and high cellularity (left panel, ×332), highest density in areas with marked cell loss and spongiotic degeneration (middle panel, ×332), and moderately high density in "burned-out" areas with near-complete cell loss (right panel; ×332). **(C)** Bar graphs depicting the comparison of histomorphometric quantitative indices between cerebellar subregions and all other CNS subregions. Top: POTV viral RNA density ($POTV_{RNA\text{-}index}$). Middle: Tissue vacuolation ($Vacuolation_{index}$). Bottom: chronic damage score (Chronic*Damage*), comprising multiple neurodegenerative histological features, including neuronal loss and tissue vacuolation. Each dot represents a sampled subregion; bars indicate group distributions. Statistical significance is shown (*p*-values indicated, Mann–Whitney U tests). **(D)** Correlation analyses within cerebellar granule cell layer (GCL) regions of interest (ROIs, $n = 108$). Scatterplots show relationships between POTV viral RNA density (ISH/μm^2), tissue vacuolation, and cellular density (cells/μm^2). Top: POTV viral RNA density vs. vacuolation (Spearman's $\rho = 0.39$, 95% CI 0.21–0.54, $p<0.0001$). Bottom: POTV viral RNA density vs. cellular density (Spearman's $\rho = -0.23$, 95% CI −0.41 to −0.038, $p = 0.016$). Each dot represents an individual annotated ROI within the GCL. Lines represent nonparametric smoothing curves (spline fit), illustrating trends in the data. Viral RNA density is positively associated with vacuolation and inversely associated with cellular density. **(E)** Hierarchical clustering of neuron-containing CNS subregions based on principal component analysis (PCA) of pathological and molecular features. Heatmap displays z-scored values of variables contributing to clustering, with dendrogram indicating relationships among regions. Cerebellar regions form a distinct cluster compared to other CNS areas.

Figure 4: Distribution of nucleotide changes across POTV genomic segments in CNS regions. Alterations to the POTV genome in the L segment (A), M segment (B), S segment N (C) and NSs (D) protein coding regions, were mapped relative to the sequence detected in cerebellar tissues (cerebellar vermis and hemispheres), which had the highest genome coverage. Variants are plotted by genomic position. Synonymous nucleotide changes are denoted with filled circles and nonsynonymous changes are denoted with opened squares. A limited number of nucleotide differences were observed across regions. Viral genomes recovered from all regions were incomplete.

References

[1]. Edridge AWD, van der Hoek L. Emerging orthobunyaviruses associated with CNS disease. PLoS Negl Trop Dis. 2020 Oct 28;14(10):e0008856.

[2]. Mitchell CJ, Smith GC, Karabatsos N, Moore CG, Francy DB, Nasci RS. Isolations of Potosi virus from mosquitoes collected in the United States, 1989-94. J Am Mosq Control Assoc. 1996 Mar;12(1):1-7.

[3]. McLean RG, Kirk LJ, Shriner RB, Cook PD, Myers EE, Gill JS, Campos EG. The role of deer as a possible reservoir host of potosi virus, a newly recognized arbovirus in the United States. J Wildl Dis. 1996 Jul;32(3):444-52.

[4]. Chiu CY, Godasi RR, Hughes HR, Servellita V, Foresythe K, Tubati A, et al. Two Human Cases of Fatal Meningoencephalitis Associated with Potosi and Lone Star Virus Infections, United States, 2020-2023. Emerg Infect Dis. 2025 Feb;31(2):215-221.

[5]. Wagner MJ, Kim TH, Savall J, Schnitzer MJ, Luo L. Cerebellar granule cells encode the expectation of reward. Nature. 2017 Apr 6;544(7648):96-100.

[6]. Wilson MR, Suan D, Duggins A, Schubert RD, Khan LM, Sample HA, Zorn KC, Rodrigues Hoffman A, Blick A, Shingde M, DeRisi JL. A novel cause of chronic viral meningoencephalitis: Cache Valley virus. Ann Neurol. 2017 Jul;82(1):105-114.

[7]. Solomon IH, Ganesh VS, Yu G, Deng XD, Wilson MR, Miller S, et al. Fatal Case of Chronic Jamestown Canyon Virus Encephalitis Diagnosed by Metagenomic Sequencing in Patient Receiving Rituximab. Emerg Infect Dis. 2021 Jan;27(1):238–42.

[8]. Yang Y, Qiu J, Snyder-Keller A, Wu Y, Sun S, Sui H, et al. Fatal Cache Valley virus meningoencephalitis associated with rituximab maintenance therapy. Am J Hematol. 2018 Aug;93(4):590-594.

[9]. Rudolph S, Badura A, Lutzu S, Pathak SS, Thieme A, Verpeut JL, et al. Cognitive-Affective Functions of the Cerebellum. J Neurosci. 2023 Nov 8;43(45):7554-7564.

[10]. Xie YY, Zhang XY, Zhu JN. The cognitive functions of the cerebellum and its role in neurodegenerative diseases. Ageing Neurodegener Dis 2024;4:18.

[11]. Mukherjee P, Woods TA, Moore RA, Peterson KE. Activation of the innate signaling molecule MAVS by bunyavirus infection upregulates the adaptor protein SARM1, leading to neuronal death. Immunity. 2013 Apr 18;38(4):705-16.

[12]. Armstrong PM, Andreadis TG, Anderson JF, Main AJ. Isolations of Potosi virus from mosquitoes (Diptera: Culicidae) collected in Connecticut. J Med Entomol. 2005 Sep;42(5):875-81.

[13]. Briese T, Kapoor V, Lipkin WI. Natural M-segment reassortment in Potosi and Main Drain viruses: implications for the evolution of orthobunyaviruses. Arch Virol. 2007;152(12):2237-47.

[14]. Luna G, Alping P, Burman J, Fink K, Fogdell-Hahn A, et al. Infection Risks Among Patients With Multiple Sclerosis Treated With Fingolimod, Natalizumab, Rituximab, and Injectable Therapies. JAMA Neurol. 2020 Feb 1;77(2):184-191.

[15]. Bennett CL, Focosi D, Socal MP, Bian JC, Nabhan C, Hrushesky WJ, Bennett AC, Schoen MW, Berger JR, Armitage JO; Southern Network on Adverse Reactions. Progressive multifocal leukoencephalopathy in patients treated with rituximab: a 20-year review from the Southern Network on Adverse Reactions. Lancet Haematol. 2021 Aug;8(8):e593-e604.

[16]. Norris LB, Georgantopoulos P, Rao GA, Sartor AO, Bennett CL. Rituximab is associated with increased risk of progressive multifocal leukoencephalopathy developing among non–HIV-infected veterans with chronic lymphocytic leukemia. J Clin Oncol. 2015;33(15_suppl):e18033. Abstract. doi:10.1200/jco.2015.33.15_suppl.e18033.
[17]. Kassab S, Saghi T, Boyer A, Lafon ME, Gruson D, Lina B, Fleury H, Schuffenecker I. Fatal case of enterovirus 71 infection and rituximab therapy, france, 2012. Emerg Infect Dis. 2013 Aug;19(8):1345-7.
[18]. Jacksch C, Dargvainiene J, Böttcher S, Diedrich S, Leypoldt F, Stürner K, Berg D, Schäffer E. Chronic Enterovirus Meningoencephalitis in Prolonged B-Cell Depletion After Rituximab Therapy: Case Report. Neurol Neuroimmunol Neuroinflamm. 2023 Oct 9;10(6):e200171.
[19]. Dang L, Dang X, Koralnik IJ, Todd PK. JC polyomavirus granule cell neuronopathy in a patient treated with rituximab. JAMA Neurol. 2014 Apr;71(4):487-9.
[20]. Li Y, Choudhary MC, Regan J, Boucau J, Nathan A, Speidel T, et al. SARS-CoV-2 viral clearance and evolution varies by type and severity of immunodeficiency. Sci Transl Med. 2024 Jan 24;16(731):eadk1599.
[21]. Hughes HR, Velez JO, Davis EH, Laven J, Gould CV, Panella AJ, et al. Fatal Human Infection with Evidence of Intrahost Variation of Eastern Equine Encephalitis Virus, Alabama, USA, 2019. Emerg Infect Dis. 2021 Jul;27(7):1886-1892.
[22]. Kapadia RK, Staples JE, Gill CM, Fischer M, Khan E, Laven JJ, et al. Severe Arboviral Neuroinvasive Disease in Patients on Rituximab Therapy: A Review. Clin Infect Dis. 2023 Mar 21;76(6):1142-1148.
[23]. Li Y, Choudhary MC, Regan J, Boucau J, Nathan A, Speidel T, et al. SARS-CoV-2 viral clearance and evolution varies by type and severity of immunodeficiency. Sci Transl Med. 2024 Jan 24;16(731):eadk1599.
[24]. Choi B, Choudhary MC, Regan J, Sparks JA, Padera RF, Qiu X, et al. Persistence and Evolution of SARS-CoV-2 in an Immunocompromised Host. N Engl J Med. 2020 Dec 3;383(23):2291-2293.
[25]. Craig M, Deng X, McLeod DV. Viral evolution during primary infection in immunocompromised hosts. PLoS Comput Biol. 2026 Feb 25;22(2):e1013967.
[26]. Weigang S, Fuchs J, Zimmer G, Schnepf D, Kern L, Beer J, et al. Within-host evolution of SARS-CoV-2 in an immunosuppressed COVID-19 patient as a source of immune escape variants. Nat Commun. 2021 Nov 4;12(1):6405.
[27]. Corey L, Beyrer C, Cohen MS, Michael NL, Bedford T, Rolland M. SARS-CoV-2 Variants in Patients with Immunosuppression. N Engl J Med. 2021 Aug 5;385(6):562-566.
[28]. Briese T, Calisher CH, Higgs S. Viruses of the family Bunyaviridae: are all available isolates reassortants? Virology. 2013 Nov;446(1-2):207-16.
[29]. McDonald SM, Nelson MI, Turner PE, Patton JT. Reassortment in segmented RNA viruses: mechanisms and outcomes. Nat Rev Microbiol. 2016 Jul;14(7):448-60. doi: 10.1038/nrmicro.2016.46.
[30]. Gerrard SR, Li L, Barrett AD, Nichol ST. Ngari virus is a Bunyamwera virus reassortant that can be associated with large outbreaks of hemorrhagic fever in Africa. J Virol. 2004 Aug;78(16):8922-6.
[31]. Briese T, Bird B, Kapoor V, Nichol ST, Lipkin WI. Batai and Ngari viruses: M segment reassortment and association with severe febrile disease outbreaks in East Africa. J Virol. 2006 Jun;80(11):5627-30.
[32]. Baker M, Hughes HR, Naqvi SH, Yates K, Velez JO, McGuirk S, et al. Reassortant Cache Valley Virus Associated With Acute Febrile, Nonneurologic Illness, Missouri. Clin Infect Dis. 2021 Nov 2;73(9):1700-1702.

[33]. Dieme C, Maffei JG, Diarra M, Koetzner CA, Kuo L, Ngo KA, et al. Aedes Albopictus and Cache Valley virus: a new threat for virus transmission in New York State. Emerg Microbes Infect. 2022 Dec;11(1):741-748.
[34]. Yousaf I, Hannon WW, Donohue RC, Pfaller CK, Yadav K, Dikdan RJ, et al. Brain tropism acquisition: The spatial dynamics and evolution of a measles virus collective infectious unit that drove lethal subacute sclerosing panencephalitis. PLoS Pathog. 2023 Dec 21;19(12):e1011817.
[35]. Stein SR, Ramelli SC, Grazioli A, Chung JY, Singh M, Yinda CK, et al. SARS-CoV-2 infection and persistence in the human body and brain at autopsy. Nature. 2022 Dec;612(7941):758-763.
[36]. Billot B, Greve DN, Puonti O, Thielscher A, Van Leemput K, Fischl B, Dalca AV, Iglesias JE; ADNI. SynthSeg: Segmentation of brain MRI scans of any contrast and resolution without retraining. Med Image Anal. 2023 May;86:102789.
[37]. Chakravarty MM, Steadman P, van Eede MC, Calcott RD, Gu V, Shaw P, Raznahan A, Collins DL, Lerch JP. Performing label-fusion-based segmentation using multiple automatically generated templates. Hum Brain Mapp. 2013 Oct;34(10):2635-54.
[38]. Park MT, Pipitone J, Baer LH, Winterburn JL, Shah Y, Chavez S, Schira MM, Lobaugh NJ, Lerch JP, Voineskos AN, Chakravarty MM. Derivation of high-resolution MRI atlases of the human cerebellum at 3T and segmentation using multiple automatically generated templates. Neuroimage. 2014 Jul 15;95:217-31.
[39]. Nakamura K, Guizard N, Fonov VS, Narayanan S, Collins DL, Arnold DL. Jacobian integration method increases the statistical power to measure gray matter atrophy in multiple sclerosis. Neuroimage Clin. 2013 Oct 29;4:10-7.
[40]. Skinner B, Mikula S, Davis BS, Powers JA, Hughes HR, Calvert AE. Monoclonal antibodies to Cache Valley virus for serological diagnosis. PLoS Negl Trop Dis. 2022 Jan 24;16(1):e0010156.
[41]. Ritter JM, Martines RB, Bhatnagar J, Rao AK, Villalba JA, Silva-Flannery L, et al. Pathology and Monkeypox virus Localisation in Tissues From Immunocompromised Patients With Severe or Fatal Mpox. J Infect Dis. 2024 Mar 26;229(Supplement_2):S219-S228.
[42]. Bhatnagar J, Gary J, Reagan-Steiner S, Estetter LB, Tong S, Tao Y, et al. Evidence of Severe Acute Respiratory Syndrome Coronavirus 2 Replication and Tropism in the Lungs, Airways, and Vascular Endothelium of Patients With Fatal Coronavirus Disease 2019: An Autopsy Case Series. J Infect Dis. 2021 Mar 3;223(5):752-764.
[43]. Bhatnagar J, Blau DM, Shieh WJ, Paddock CD, Drew C, Liu L, Jones T, Patel M, Zaki SR. Molecular detection and typing of dengue viruses from archived tissues of fatal cases by rt-PCR and sequencing: diagnostic and epidemiologic implications. Am J Trop Med Hyg. 2012 Feb;86(2):335-40.
[44]. Shieh WJ, Blau DM, Denison AM, Deleon-Carnes M, Adem P, Bhatnagar J, Sumner J, Liu L, Patel M, Batten B, Greer P, Jones T, Smith C, Bartlett J, Montague J, White E, Rollin D, Gao R, Seales C, Jost H, Metcalfe M, Goldsmith CS, Humphrey C, Schmitz A, Drew C, Paddock C, Uyeki TM, Zaki SR. 2009 pandemic influenza A (H1N1): pathology and pathogenesis of 100 fatal cases in the United States. Am J Pathol. 2010 Jul;177(1):166-75.
[45]. Meuten DJ, Moore FM, George JW. Mitotic Count and the Field of View Area: Time to Standardize. Vet Pathol. 2016 Jan;53(1):7-9.
[46]. Schmidt U, Weigert M, Broaddus C, Myers G. Cell detection with star-convex polygons. In: Frangi AF, Schnabel JA, Davatzikos C, Alberola-López C, Fichtinger G, eds. Medical Image Computing and Computer-Assisted Intervention — MICCAI 2018. Cham, Switzerland: Springer; 2018:265-273.
[47]. Bankhead P, Loughrey MB, Fernández JA, Dombrowski Y, McArt DG, Dunne PD, et al. QuPath: Open source software for digital pathology image analysis. Sci Rep. 2017 Dec 4;7(1):16878.

[48]. Davis E, Velez J, Hamik J, Fitzpatrick K, Haley J, Eschliman J, et al. Evidence of Lineage 1 and 3 West Nile Virus in Person with Neuroinvasive Disease, Nebraska, USA, 2023. Emerg Infect Dis. 2024 Oct;30(10):2090-2098.

Acknowledgements

We thank Ms. Amy Morris and Ms. Rhonda Cole for performing histology and histochemical staining, and Dr. Hannah Bullock for critically reviewing the manuscript.

Role of the funding source

Authors did not receive specific funding for this study. The data in this study are collected and managed by the US CDC; however, the corresponding author had full access to all the data in the study and had the final responsibility for the decision to submit for publication.

Disclaimer

The findings and conclusions in this report are those of the authors and do not necessarily represent the official position of the Centers for Disease Control and Prevention.

Contributions

J.A.V. and J.B. conceived the study and designed experiments. E.D., K.N., J.B., A.C.B., H.R.H., A.E.C., G.F., S.CC, P.F., M.DL.C., T.L., J.R.A., and R.J.F. helped with experimental design or performed experiments. G.A.Y performed the postmortem examination. J.R.A., C.I., H.W., S.A.M, and R.J.F. provided patient care, collected antemortem samples, or provided clinical data. J.A.V, J.K., G.A.Y., M.L.C, and P.LP. performed histopathological evaluation of postmortem samples. C.V.G., B.L., K.D.N., J.E.S, H.W., and G.A.Y. provided epidemiological coordination, and assisted in specimen shipping. C.V.G., and J.E.S provided expert clinical consultation. E.D., A.E.C., G.F., S.CC, P.F., M.DL.C., T.L., and H.R.H. performed specimen testing or assisted with technical analysis/interpretation. J.A.V. performed histopathological quantitative and semiquantitative analyses. J.A.V. provided domain knowledge guiding algorithm generation. K.S. developed machine-learning algorithms. K.N. performed MRI image analyses. S.A.M, and S.D. were responsible for clinical mNGS testing analyses and interpretation. J.A.V., J.B., T.L., M.DL.C., E.D., K.S. and K.N. were responsible for data analysis. J. A. V. wrote the manuscript, with input from all authors. All authors reviewed and approved the manuscript.

Corresponding author

Correspondence to Julian A. Villalba.

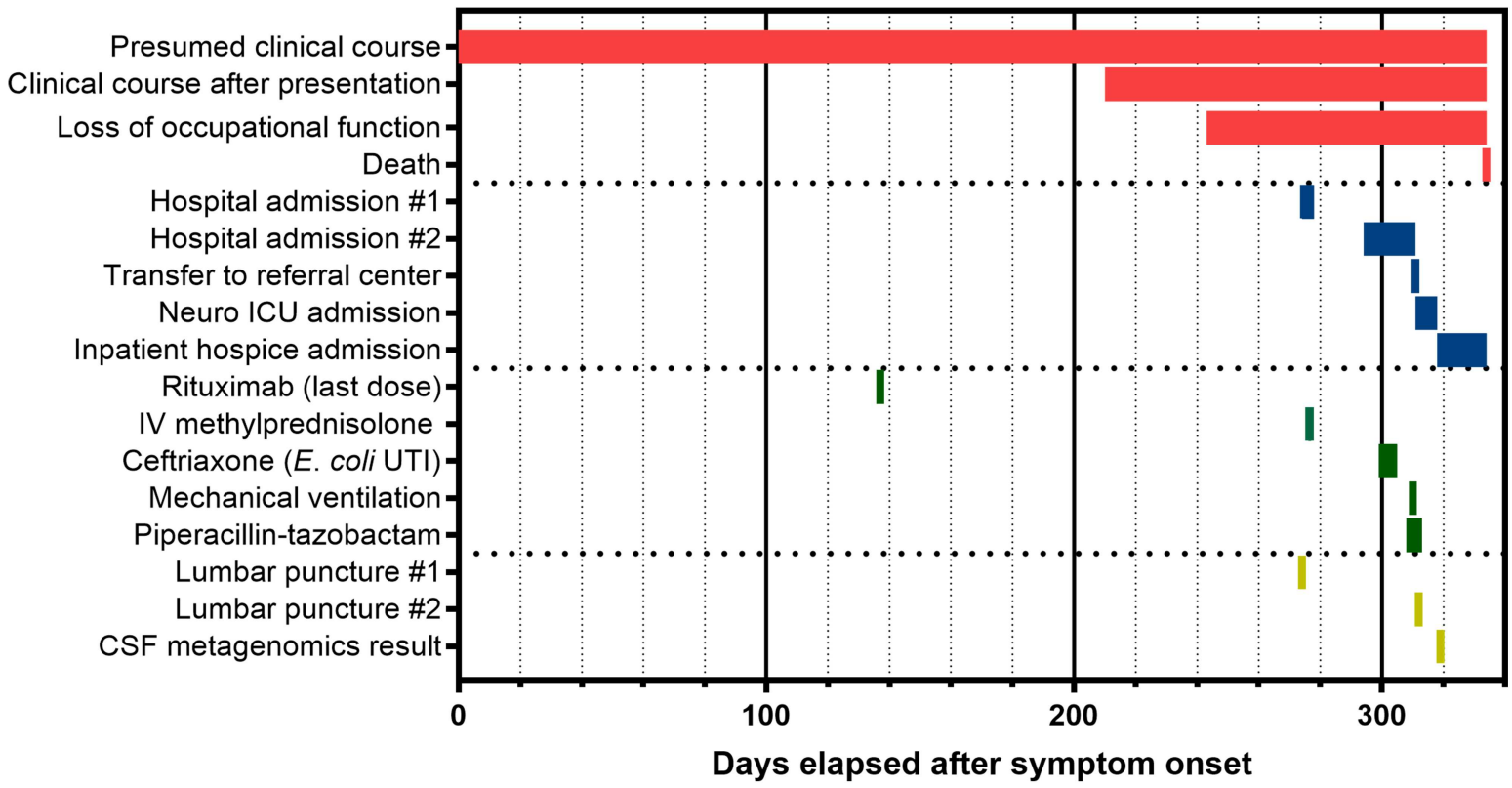
Data availability

All data are available from the corresponding author upon reasonable request.

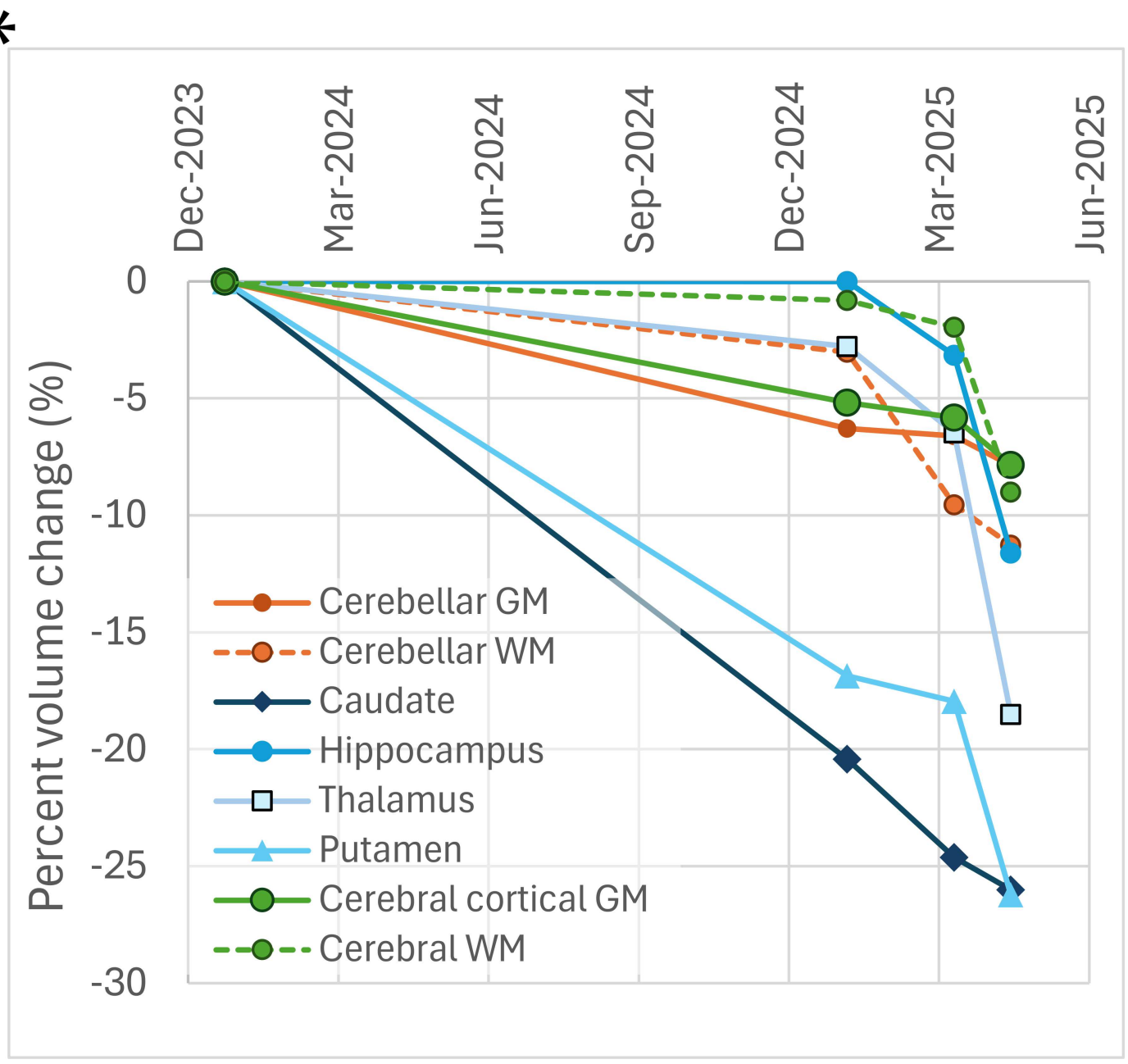
Code availability

All codes are available from the corresponding author upon reasonable request.

a

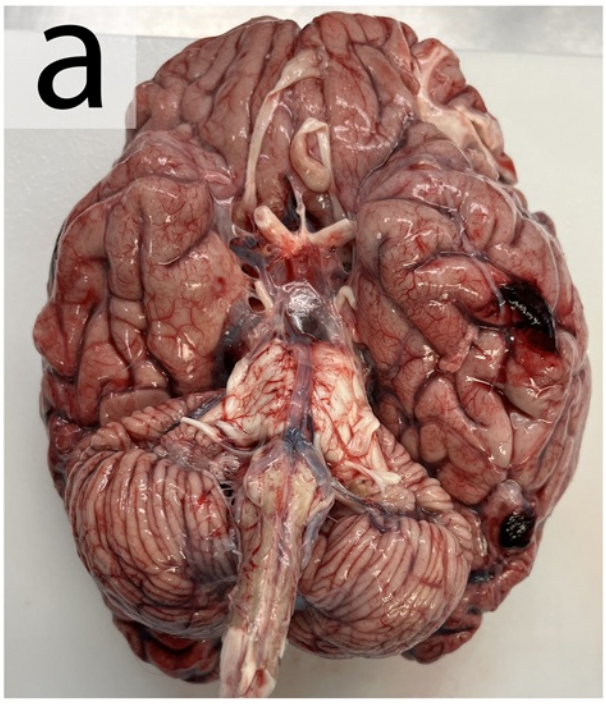

Presumed clinical course
Clinical course after presentation
Loss of occupational function
Death
Hospital admission #1
Hospital admission #2
Transfer to referral center
Neuro ICU admission
Inpatient hospice admission
Rituximab (last dose)
IV methylprednisolone
Ceftriaxone (E. coli UTI)
Mechanical ventilation
Piperacillin-tazobactam
Lumbar puncture #1
Lumbar puncture #2
CSF metagenomics result
0
100
200
300
Days elapsed after symptom onset

b

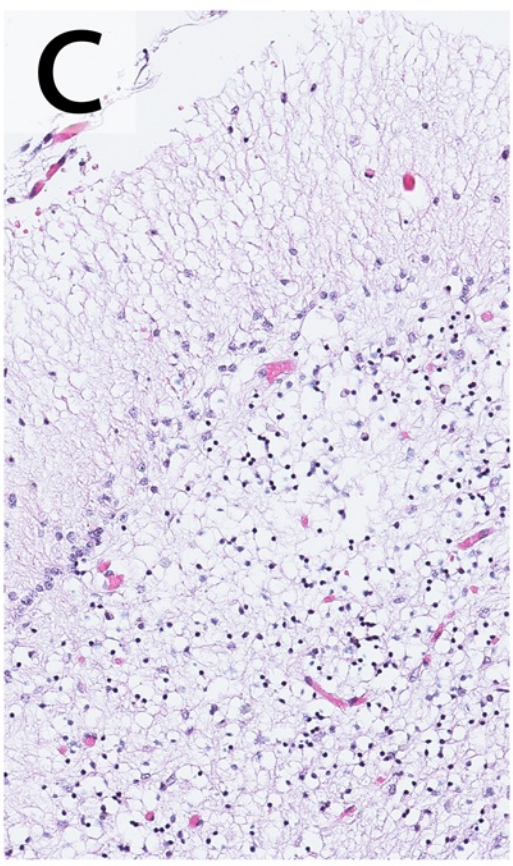

*
Dec-2023
Mar-2024
Jun-2024
Sep-2024
Dec-2024
Mar-2025
Jun-2025
0
-5
-10
-15
-20
-25
-30
Percent volume change (%)
Cerebellar GM
Cerebellar WM
Caudate
Hippocampus
Thalamus
Putamen
Cerebral cortical GM
Cerebral WM

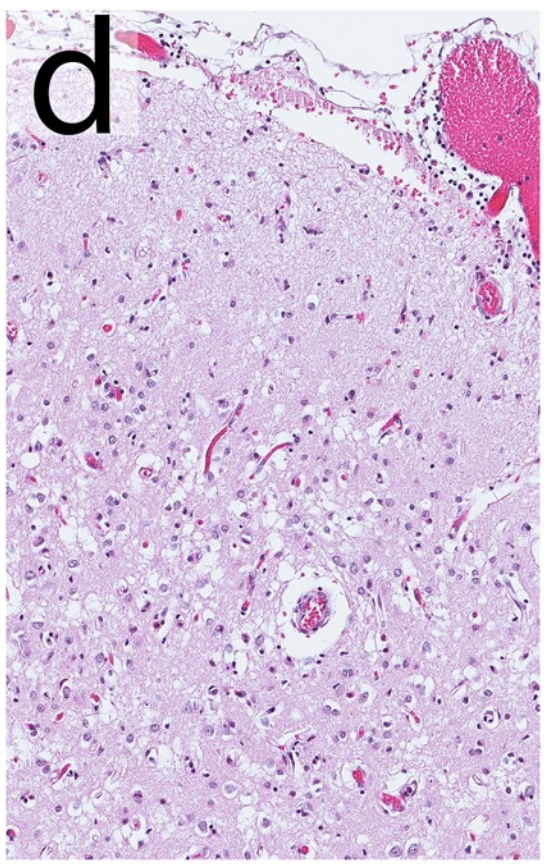
C

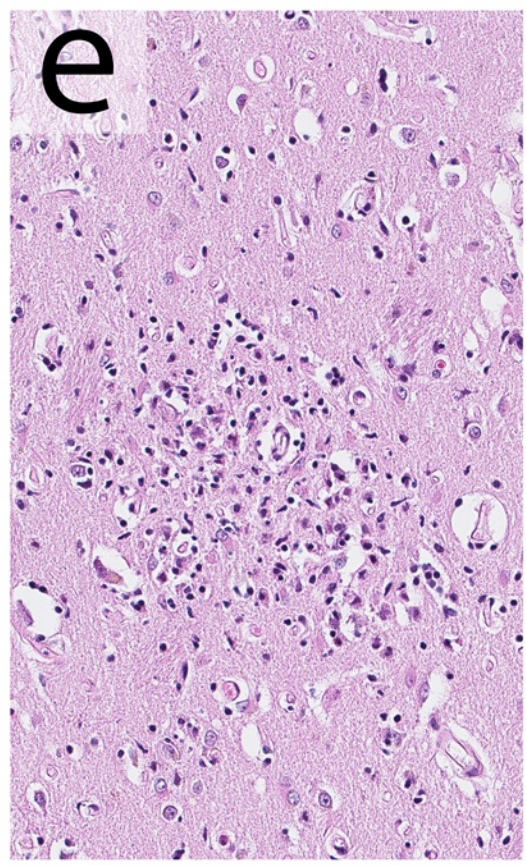
Proportion of total volume loss (%)
2024/01 - 2025/01
2025/01 - 2025/04
2025/04 - 2025/05
Cerebellar grey matter 80 4 16
Caudate nucleus 79 16 5
Cerebral cortical grey matter 66 8 26
Putamen 64 4 32
Cerebellar white matter 27 58 15
Thalamus 15 20 65
Hippocampus 0 27 73
Cerebral white matter 9 13 78
90 - 100
80 - 89
70 - 79
60 - 69
50 - 59
40 - 49
30 - 39
20 - 29
10 - 19
1 - 9
0

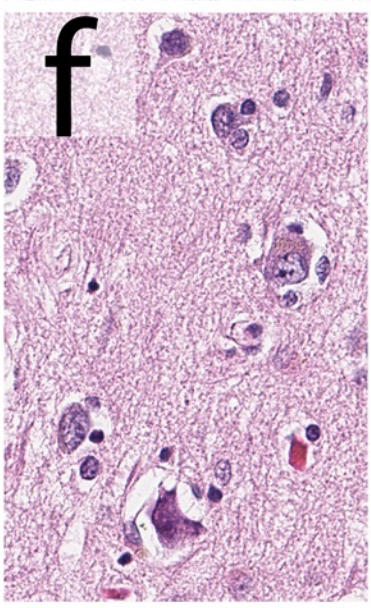


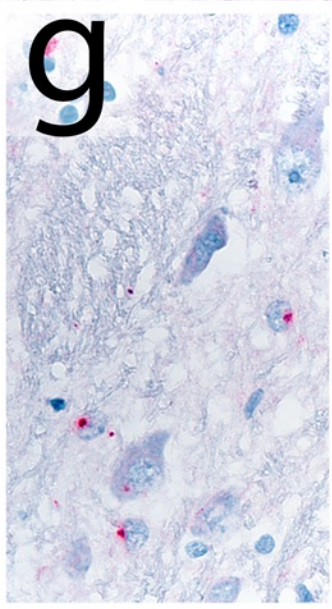


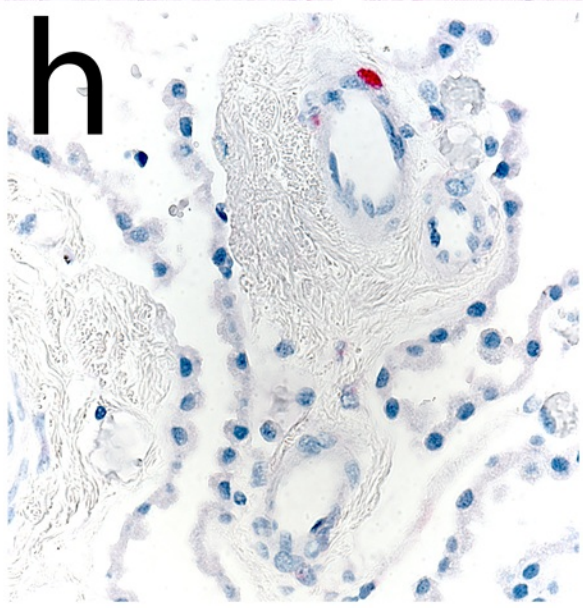


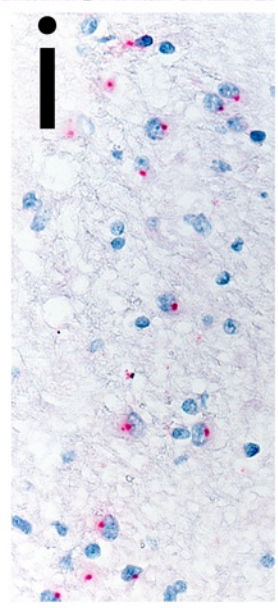












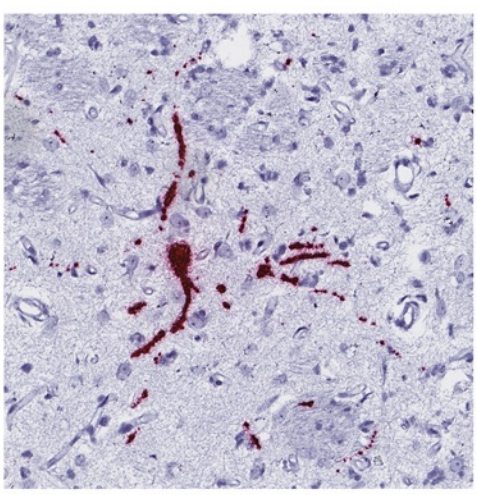
j

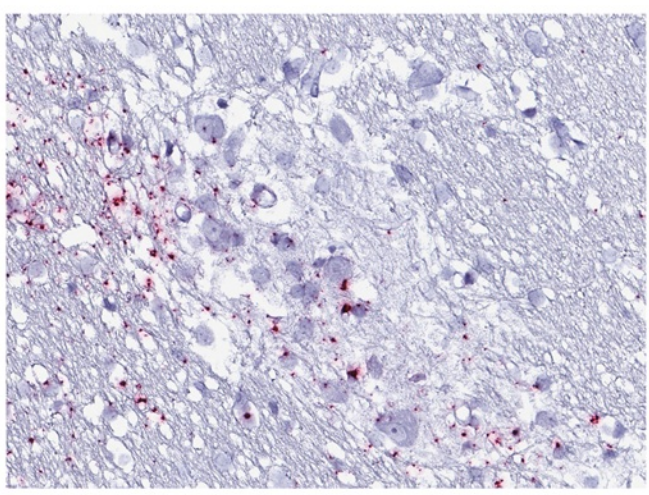
In-situ Hybridization

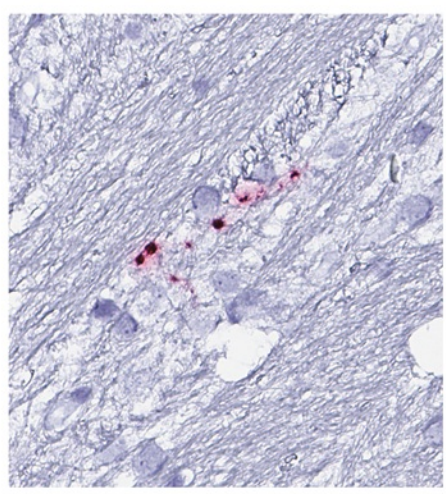
S gene segment - sense

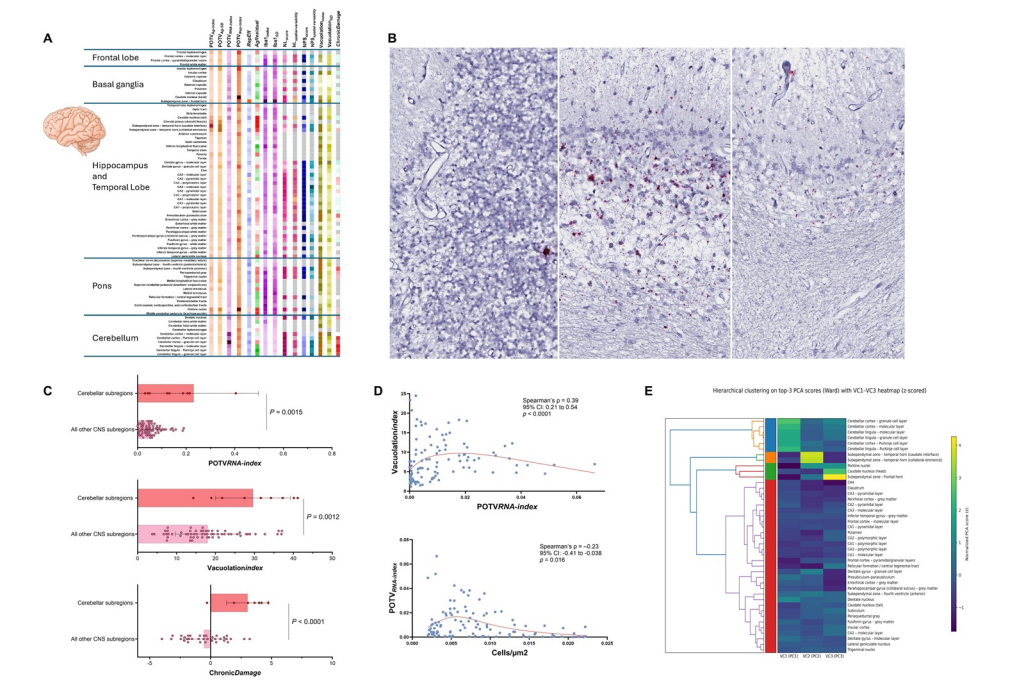
L gene segment - sense

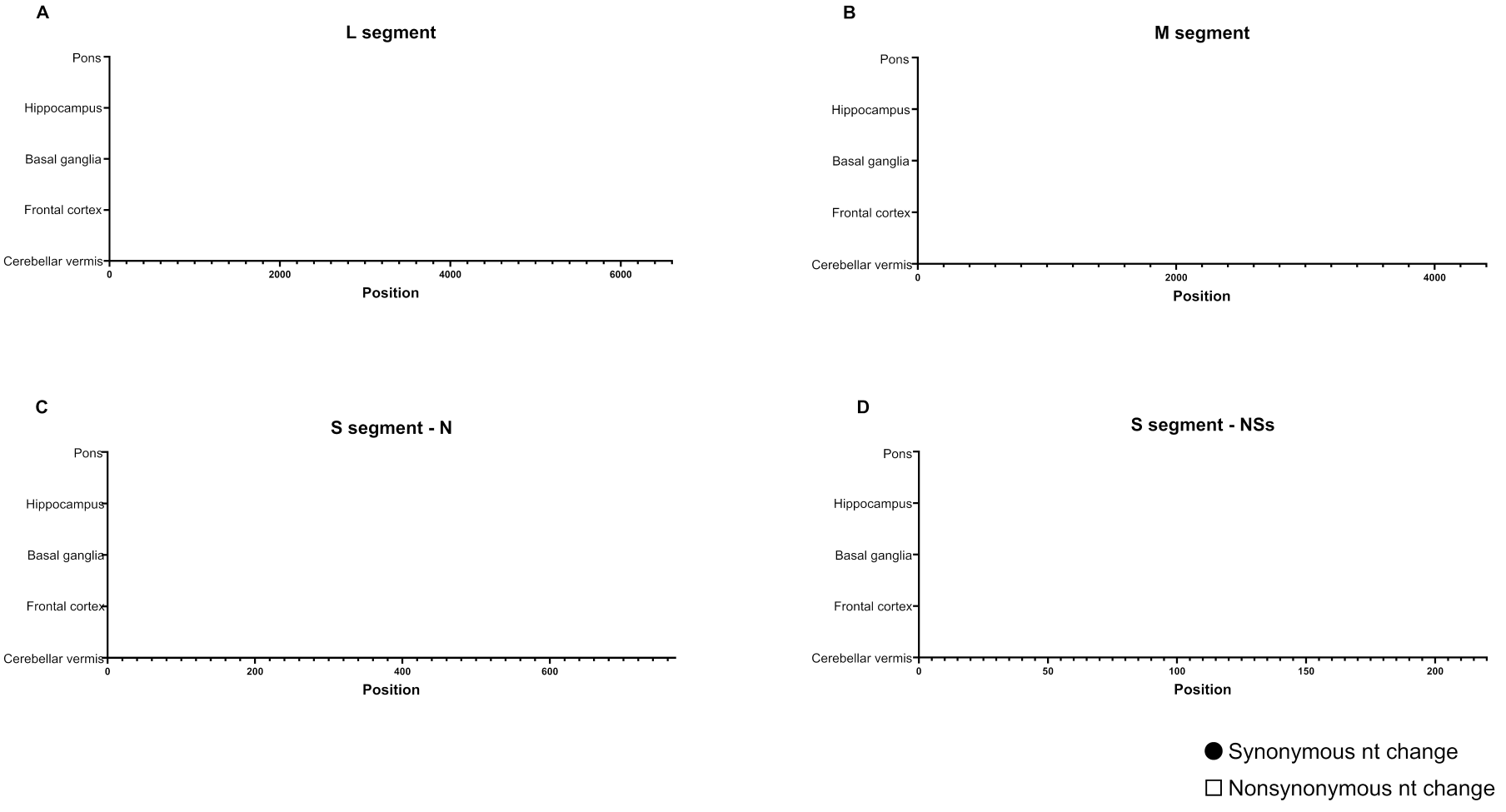
L gene segment - antisense








A
Frontal lobe
Basal ganglia
Hippocampus and Temporal Lobe
Pons
Cerebellum
POTVmRNA-index
POTVRNA-index
POTVmiRNA-index
Vacuolation-index
Perivascular
Parenchymal
Astrocytic
Glial
Neuronal
Vascular
Mixed
NM Neuronal-vascularity
WM Neuronal-vascularity
Vacuolation-index
Vacuolation-type
ChronicDamage
B
C
Cerebellar subregions
All other CNS subregions
P = 0.0015
POTVRNA-index
P = 0.0012
Vacuolation-index
P < 0.0001
ChronicDamage
D
Spearman's ρ = 0.39
95% CI: 0.21 to 0.54
p < 0.0001
Vacuolation-index
POTVRNA-index
Spearman's ρ = −0.23
95% CI: -0.41 to -0.038
p = 0.016
POTVmiRNA-index
Cells/µm2
E
Hierarchical clustering on top-3 PCA scores (Ward) with VC1-VC3 heatmap (z-scored)
VC1 (PC1)
VC2 (PC2)
VC3 (PC3)
Normalized PCA score (z)


A
L segment
Pons
Hippocampus
Basal ganglia
Frontal cortex
Cerebellar vermis
0
2000
4000
6000
Position
B
M segment
Pons
Hippocampus
Basal ganglia
Frontal cortex
Cerebellar vermis
0
2000
4000
Position
C
S segment - N
Pons
Hippocampus
Basal ganglia
Frontal cortex
Cerebellar vermis
0
200
400
600
Position
D
S segment - NSs
Pons
Hippocampus
Basal ganglia
Frontal cortex
Cerebellar vermis
0
50
100
150
200
Position
Synonymous nt change
Nonsynonymous nt change

Supplementary Files

This is a list of supplementary files associated with this preprint. Click to download.

- Appendixv3.1cleanBTX6NM.docx
- machinelearning.pdf
- rsnew.pdf